



Two New HATNet Hot Jupiters around A Stars and the First Glimpse at the Occurrence Rate of Hot Jupiters from *TESS**

G. Zhou^{1,44} , C. X. Huang² , G. Á. Bakos^{3,4,45,48} , J. D. Hartman³ , David W. Latham¹ , S. N. Quinn¹ , K. A. Collins¹ , J. N. Winn³ , I. Wong^{5,46} , G. Kovács⁶, Z. Csabry³, W. Bhatti³ , K. Penev⁷ , A. Bieryla¹ , G. A. Esquerdo¹, P. Berlind¹, M. L. Calkins¹ , M. de Val-Borro⁸, R. W. Noyes¹, J. Lázár⁹, I. Papp⁹, P. Sári⁹, T. Kovács⁶ , Lars A. Buchhave¹⁰ , T. Szklenar⁹, B. Béky¹¹, M. C. Johnson¹² , W. D. Cochran¹³ , A. Y. Kniazev^{14,15} , K. G. Stassun^{16,17} , B. J. Fulton¹⁸ , A. Shporer² , N. Espinoza^{19,20,21} , D. Bayliss²² , M. Everett²³ , S. B. Howell²⁴ , C. Hellier²⁵ , D. R. Anderson^{22,25} , A. Collier Cameron²⁶, R. G. West²², D. J. A. Brown²² , N. Schanche²⁶ , K. Barkaoui^{27,28}, F. Pozuelos²⁹ , M. Gillon²⁷ , E. Jehin²⁹, Z. Benkhaldoun²⁸, A. Daassou²⁸, G. Ricker², R. Vanderspek² , S. Seager^{2,5,30}, J. M. Jenkins²⁴ , Jack J. Lissauer²⁴, J. D. Armstrong³¹, K. I. Collins¹⁶, T. Gan³², R. Hart³³, K. Horne²⁶ , J. F. Kielkopf³⁴, L. D. Nielsen³⁵, T. Nishiumi³⁶, N. Narita^{37,38,39,40,41} , E. Palle^{41,42}, H. M. Relles¹, R. Sefako¹⁴, T. G. Tan⁴³ , M. Davies²⁴, Robert F. Goeke², N. Guerrero², K. Haworth², and S. Villanueva^{2,47}

¹ Center for Astrophysics | Harvard & Smithsonian, 60 Garden Street, Cambridge, MA 02138, USA; george.zhou@cfa.harvard.edu

² Department of Physics, and Kavli Institute for Astrophysics and Space Research, Massachusetts Institute of Technology, Cambridge, MA 02139, USA

³ Department of Astrophysical Sciences, Princeton University, NJ 08544, USA

⁴ Konkoly Observatory, Hungary

⁵ Department of Earth, Atmospheric and Planetary Sciences, Massachusetts Institute of Technology, Cambridge, MA 02139, USA

⁶ Konkoly Observatory of the Hungarian Academy of Sciences, Budapest, 1121 Konkoly Thege ut. 15-17, Hungary

⁷ Physics Department, University of Texas at Dallas, 800 W Campbell Road MS WT15, Richardson, TX 75080, USA

⁸ Astrochemistry Laboratory, Goddard Space Flight Center, NASA, 8800 Greenbelt Road, Greenbelt, MD 20771, USA

⁹ Hungarian Astronomical Association, 1451 Budapest, Hungary

¹⁰ DTU Space, National Space Institute, Technical University of Denmark, Elektrovej 328, DK-2800 Kgs. Lyngby, Denmark

¹¹ Google Inc, USA

¹² Department of Astronomy, The Ohio State University, 140 West 18th Avenue, Columbus, OH 43210, USA

¹³ McDonald Observatory, University of Texas at Austin, 2515 Speedway, Stop C1400, Austin, TX 78712, USA

¹⁴ South African Astronomical Observatory, PO Box 9, 7935 Observatory, Cape Town, South Africa

¹⁵ Southern African Large Telescope Foundation, PO Box 9, 7935 Observatory, Cape Town, South Africa

¹⁶ Department of Physics and Astronomy, Vanderbilt University, 6301 Stevenson Center, Nashville, TN 37235, USA

¹⁷ Department of Physics, Fisk University, 1000 17th Avenue North, Nashville, TN 37208, USA

¹⁸ Caltech/IPAC-NExScI, 1200 East California Boulevard, Pasadena, CA 91125, USA

¹⁹ Max-Planck-Institut für Astronomie, Königstuhl 17, D-69117 Heidelberg, Germany

²⁰ Instituto de Astrofísica, Facultad de Física, Pontificia Universidad Católica de Chile, Av. Vicuña Mackenna 4860, 782-0436 Macul, Santiago, Chile

²¹ Millennium Institute of Astrophysics (MAS), Av. Vicuña Mackenna 4860, 782-0436 Macul, Santiago, Chile

²² Department of Physics, University of Warwick, Gibbet Hill Road, Coventry CV4 7AL, UK

²³ National Optical Astronomy Observatory, Tucson, AZ, USA

²⁴ NASA Ames Research Center, Moffett Field, CA 94035, USA

²⁵ Astrophysics Group, Keele University, Staffordshire, ST5 5BG, UK

²⁶ SUPA, School of Physics and Astronomy, University of St. Andrews, North Haugh, Fife, KY16 9SS, UK

²⁷ Astrobiology Research Unit, University of Liège, Belgium

²⁸ Oukaimeden Observatory, High Energy Physics and Astrophysics Laboratory, Cadi Ayyad University, Marrakech, Morocco

²⁹ Space Sciences, Technologies and Astrophysics Research (STAR) Institute, University of Liège, Belgium

³⁰ Department of Aeronautics and Astronautics, MIT, 77 Massachusetts Avenue, Cambridge, MA 02139, USA

³¹ Institute for Astronomy, University of Hawaii, 34 Ohia Ku Street, Pukalani, Maui, HI 96768, USA

³² Physics Department and Tsinghua Centre for Astrophysics, Tsinghua University, Beijing 100084, People's Republic of China

³³ Centre for Astrophysics, University of Southern Queensland, Toowoomba, QLD, 4350, Australia

³⁴ Department of Physics and Astronomy, University of Louisville, Louisville, KY 40292, USA

³⁵ Observatoire de Genève, Université de Genève, 51 Chemin des Maillettes, 1290 Sauverny, Switzerland

³⁶ Kyoto Sangyo University, Motoyama, Kamigamo, Kita-Ku, Kyoto-City, 603-8555, Japan

³⁷ Department of Astronomy, The University of Tokyo, 7-3-1 Hongo, Bunkyo-ku, Tokyo 113-0033, Japan

³⁸ Astrobiology Center, 2-21-1 Osawa, Mitaka, Tokyo 181-8588, Japan

³⁹ JST, PRESTO, 7-3-1 Hongo, Bunkyo-ku, Tokyo 113-0033, Japan

⁴⁰ National Astronomical Observatory of Japan, 2-21-1 Osawa, Mitaka, Tokyo 181-8588, Japan

⁴¹ Instituto de Astrofísica de Canarias (IAC), E-38205 La Laguna, Tenerife, Spain

⁴² Departamento de Astrofísica, Universidad de La Laguna (ULL), E-38206, La Laguna, Tenerife, Spain

⁴³ Perth Exoplanet Survey Telescope, Perth, Western Australia

Received 2019 June 2; revised 2019 July 26; accepted 2019 July 28; published 2019 September 11

* Based on observations obtained with the Hungarian-made Automated Telescope Network. Based in part on observations obtained with the Tillinghast Reflector 1.5 m telescope and the 1.2 m telescope, both operated by the Smithsonian Astrophysical Observatory at the Fred Lawrence Whipple Observatory in Arizona. This work makes use of the Smithsonian Institution High Performance Cluster (SI/HPC). Based in part on observations made with the Southern African Large Telescope (SALT).

⁴⁴ Hubble Fellow.

⁴⁵ Packard Fellow.

⁴⁶ 51 Pegasi b Fellow.

⁴⁷ Pappalardo Fellow.

⁴⁸ MTA Distinguished Guest Fellow.

Abstract

Wide-field surveys for transiting planets are well suited to searching diverse stellar populations, enabling a better understanding of the link between the properties of planets and their parent stars. We report the discovery of HAT-P-69 b (TOI 625.01) and HAT-P-70 b (TOI 624.01), two new hot Jupiters around A stars from the Hungarian-made Automated Telescope Network (HATNet) survey that have also been observed by the *Transiting Exoplanet Survey Satellite*. HAT-P-69 b has a mass of $3.58^{+0.58}_{-0.58} M_{\text{Jup}}$ and a radius of $1.676^{+0.051}_{-0.033} R_{\text{Jup}}$ and resides in a prograde 4.79 day orbit. HAT-P-70 b has a radius of $1.87^{+0.15}_{-0.10} R_{\text{Jup}}$ and a mass constraint of $<6.78 (3\sigma) M_{\text{Jup}}$ and resides in a retrograde 2.74 day orbit. We use the confirmation of these planets around relatively massive stars as an opportunity to explore the occurrence rate of hot Jupiters as a function of stellar mass. We define a sample of 47,126 main-sequence stars brighter than $T_{\text{mag}} = 10$ that yields 31 giant planet candidates, including 18 confirmed planets, 3 candidates, and 10 false positives. We find a net hot Jupiter occurrence rate of $0.41 \pm 0.10\%$ within this sample, consistent with the rate measured by *Kepler* for FGK stars. When divided into stellar mass bins, we find the occurrence rate to be $0.71 \pm 0.31\%$ for G stars, $0.43 \pm 0.15\%$ for F stars, and $0.26 \pm 0.11\%$ for A stars. Thus, at this point, we cannot discern any statistically significant trend in the occurrence of hot Jupiters with stellar mass.

Key words: planetary systems – stars: individual (HAT-P-69, HAT-P-70, TIC379929661, TIC399870368) – techniques: photometric – techniques: spectroscopic

Supporting material: machine-readable tables

1. Introduction

Radial velocity and transit surveys have been responsible for the discovery of about 400 close-in giant planets with periods less than 10 days.⁴⁹ These “hot Jupiters” are the best-characterized exoplanets and are test beds for nearly all of the techniques to measure the densities, composition, atmospheres, orbital, and dynamical properties of exoplanetary systems. Hot Jupiters are also extreme examples of planetary migration, thought to have formed beyond the ice line, and migrated to their present-day locations via interactions with the protoplanetary gas disk, or via dynamical interactions with nearby planets or stars followed by tidal migration (as recently reviewed by Dawson & Johnson 2018).

About three-quarters of the known hot Jupiters have emerged from ground-based, wide-field transit surveys. These surveys have been successful not only in detecting a large number of planets, but also in searching a wide range of stellar types, thanks to their wide-field sky coverage. Transiting Jovian planets have been confirmed around stars ranging from M dwarfs (HATS-6, Hartman et al. 2015; NGTS-1, Bayliss et al. 2018; HATS-71, Bakos et al. 2018) to A stars (e.g., WASP-33, Collier Cameron et al. 2010; KELT-9, Gaudi et al. 2017).

The properties of planets are thought to be dependent on the properties of the host stars. In particular, more massive stars may host more massive protoplanetary disks (e.g., Natta et al. 2006). Radial velocity surveys of intermediate-mass subgiants (“retired A stars”) reported that giant planets are more abundant around more massive stars, but tend to have wider and more circular orbits than their lower-mass main-sequence counterparts (Johnson et al. 2010; Jones et al. 2014; Reffert et al. 2015; Ghezzi et al. 2018). Data from the *Kepler* primary mission allowed for the determination of occurrence rates for planets as small as $1 R_{\oplus}$ around FGK stars (e.g., Howard et al. 2012; Dong & Zhu 2013; Fressin et al. 2013; Petigura et al. 2013; Burke et al. 2015; Petigura et al. 2018). In particular, occurrence rates from *Kepler* indicate that small planets with orbital periods less than a year are more common around less massive stars (Dressing & Charbonneau 2013; Mulders et al. 2015).

Despite this progress, many questions remain unanswered. Planets around main-sequence A stars are still poorly explored. A stars have radii as large as $4 R_{\odot}$ on the main sequence, causing the transit depth of a Jovian planet to be 16 times smaller than it would be for a solar-type star. As such, ground-based transit surveys have poor completeness in this regime. The *Kepler* mission could have performed a sensitive search for giant planets around A stars, but in fact very little data from main-sequence A stars were obtained, because the mission was geared toward the detection of smaller planets for which FGK stars are more favorable. For these reasons, there has been no robust determination of the frequency of giant planets around main-sequence A stars.

There has also been tension between the occurrence rates of hot Jupiters measured by *Kepler* ($0.43 \pm 0.05\%$ from Fressin et al. 2013, $0.57^{+0.14}_{-0.12}\%$ from Petigura et al. 2018, $0.43^{+0.07}_{-0.06}\%$ from Masuda & Winn 2017) and those from radial velocity surveys ($1.5 \pm 0.6\%$ from Cumming et al. 2008, $1.2 \pm 0.4\%$ from Wright et al. 2012). These differences have been attributed to metallicity (e.g., Wright et al. 2012), stellar age, or multiplicity (Wang et al. 2015, although see also Bouma et al. 2018). Surveying different populations with a diverse set of host stars may help resolve these tensions.

The launch of the *Transiting Exoplanet Survey Satellite* (*TESS*; Ricker et al. 2016) heralds a new era of exoplanet characterization. In particular, the 30 minute cadence Full Frame Images (FFI) are providing us with an opportunity to search a wide range of stellar types. Unlike *Kepler*, with *TESS* there is no need to preselect the target stars to be within a certain range of masses or sizes. Based on observations of seven sky sectors between late 2018 July and 2019 February, *TESS* has delivered space-based photometry for 126,950 stars brighter than $T_{\text{mag}} = 10$. The promise of near-complete sensitivity from space-based photometry to hot Jupiters across the main sequence and the availability of follow-up results from the tremendous efforts of the *TESS* follow-up program motivate another look into the occurrence rates of hot Jupiters.

In this paper, we describe the confirmation of two planets discovered by the Hungarian-made Automated Telescope Network (HATNet) survey around A stars, members of a relatively unexplored planet demographic. *TESS* data for these objects became available during our confirmation process and

⁴⁹ NASA Exoplanet Archive, 2019 April.

were independently identified as planet candidates based on FFI photometry. The follow-up observations, modeling of the systems, and derived system parameters are described in Sections 2 and 3. In Section 4, we describe our estimates of the occurrence rates of hot Jupiters around main-sequence A, F, and G stars. The estimate makes use of a magnitude-limited sample of main-sequence stars ($T_{\text{mag}} < 10$) surveyed by *TESS* during its first seven sectors, planets cataloged in the *TESS* Objects of Interest (TOI) list, existing planets from the literature recovered by *TESS*, and false-positive rates estimated via vetting observations of the *TESS* follow-up program.

2. Observations

HAT-P-69 and HAT-P-70 were identified as transiting planet candidates by the HATNet survey (Bakos et al. 2004). HAT-P-69 was observed by HATNet between 2010 November and 2011 June, resulting in approximately 24,000 photometric data points. Subsequently, it received photometric and spectroscopic follow-up observations over 2011–2019 that confirmed its planetary nature. It was then observed during Sector 7 of the *TESS* mission, flagged as a transiting planet candidate by the MIT quick-look pipeline (C. X. Huang et al. 2019, in preparation), and assigned TOI number 625. These highly precise space-based photometric observations are subsequently incorporated in the analyses below. HAT-P-69 was also independently identified as a planet candidate (1SWASPJ084201.35+034238.0) by the Wide Angle Search for Planets (WASP) survey (Pollacco et al. 2006) and was the subject of extensive photometric follow-up via the WASP survey team. These observations are described in Section 2.1 and included in the global analyses.

HAT-P-70 was identified as a planet candidate based on nearly 10,000 HATNet observations spanning the interval from 2009 September to 2010 March. Subsequent ground-based photometric follow-up observations were attempted during the 2016–2017 time frame, but these observations failed to recover the transit event due to the accumulation of uncertainty in the transit ephemerides. HAT-P-70 was also independently identified as a hot Jupiter candidate by the Massachusetts Institute of Technology (MIT) quick-look pipeline and given the designation TOI 624. The revised ephemeris from *TESS* allowed us to successfully perform photometric and spectroscopic follow-up observations that confirmed the planetary nature of the system. HAT-P-70 was also identified by the WASP survey independently as a planet candidate (1SWASPJ045812.56+095952.7), receiving substantial ground-based photometric follow-up prior to the *TESS* observations.

2.1. Photometry

2.1.1. Candidate Identification by HATNet

The HATNet survey (Bakos et al. 2004) is one of the longest-running wide-field photometric surveys for transiting planets. It employs a network of small robotic telescopes at the Fred Lawrence Whipple Observatory (FLWO) in Arizona and at Maunakea Observatory in Hawaii. Each survey field is $8^\circ \times 8^\circ$, and observations are obtained with the Sloan r' filter. Observations are reduced following the process laid out by Bakos et al. (2010). Light curves were extracted via aperture photometry. Systematic effects were mitigated using external parameter decorrelation (EPD; Bakos et al. 2007), and the trend

filtering algorithm (TFA; Kovács et al. 2005). Periodic transit signals were identified via the box-fitting least squares analysis (BLS; Kovács et al. 2002). The HATNet observations are summarized in Table 1, and the discovery light curves are shown in Figure 1.

2.1.2. *TESS* Observations

HAT-P-69 and HAT-P-70 were observed by *TESS* during Year 1 of its primary mission. HAT-P-69 is present in the Camera 1 FFIs obtained during the Sector 7 campaign, between 2019 January 7 and February 2. HAT-P-70 is present on the Camera 1 FFIs in Sector 5, between 2018 November 15 and December 11. *TESS* FFIs provide approximately 27 days of nearly continuous monitoring for all stars within its field of view.

We extracted the FFI light curves of the two systems with the *lightcurve* package (Barentsen et al. 2019) using the public FFI images from the Mikulski Archive for Space Telescopes (MAST) archive produced from the Science Processing Operations Center pipeline (Jenkins et al. 2016). The raw aperture photometry light curves are diluted by the presence of nearby bright stars. In particular, HAT-P-70 is located within $33''$ (1.6 pixels) of a fainter star with a magnitude difference of $\Delta T_{\text{mag}} = 0.75$. We extracted 10×10 pixel subrasters surrounding each star and defined photometric apertures to include all pixels with fluxes higher than 68% of the fluxes of nearby pixels. For HAT-P-70, this aperture includes both the target star and the nearby neighbor. For HAT-P-69, the photometric aperture does not contain any other stars within 6 mag of the target star. Nearby pixels of apparently blank sky were used to estimate the background flux surrounding the target star. Figure 2 shows each star as observed by *TESS*, along with the photometric aperture. An R -band image of the star field from the Digitized Sky Survey 2 (McLean et al. 2000) is also shown for reference. The extracted light curve of HAT-P-70 was then deblended, based on the magnitudes of nearby stars from version 6 of the *TESS* Input Catalog (Stassun et al. 2018).

Figures 3 and 4 present the *TESS* light curves of the target stars. The *TESS* light curves of HAT-P-69 and HAT-P-70 show no large systematic variation, nor signs of pulsations or additional eclipsing companions. The *TESS* transit signals agree in depth with the depths that are measured from ground-based observations.

Phase Modulation and Secondary Eclipses—Hot Jupiters on circular orbits are expected to be tidally locked (e.g., Mazeh 2008), with a fixed dayside atmosphere facing the star at all times. As a result, there can be large temperature differences between the dayside and nonilluminated nightside. During a secondary eclipse, when the planet passes behind the star, the total flux from the dayside is occulted. In addition, as the planet orbits the host star, the flux from the planet’s sky-projected hemisphere changes periodically, producing an atmospheric brightness modulation.

To search for these signals in the *TESS* data, we fit a simple phase curve model to the full light curve (transits, secondary eclipses, and out-of-eclipse flux modulation), following the methods described in detail in Shporer et al. (2019). Given the geometry of the system, the extrema of the atmospheric brightness modulation occur during conjunction, that is, a cosine of the orbital phase. The out-of-eclipse flux is therefore given by $F(t) = 1 + B_1 \cos(\phi)$, where $\phi = 2\pi(t - T_c)$ is the orbital phase, and B_1 is the semiamplitude of the phase curve

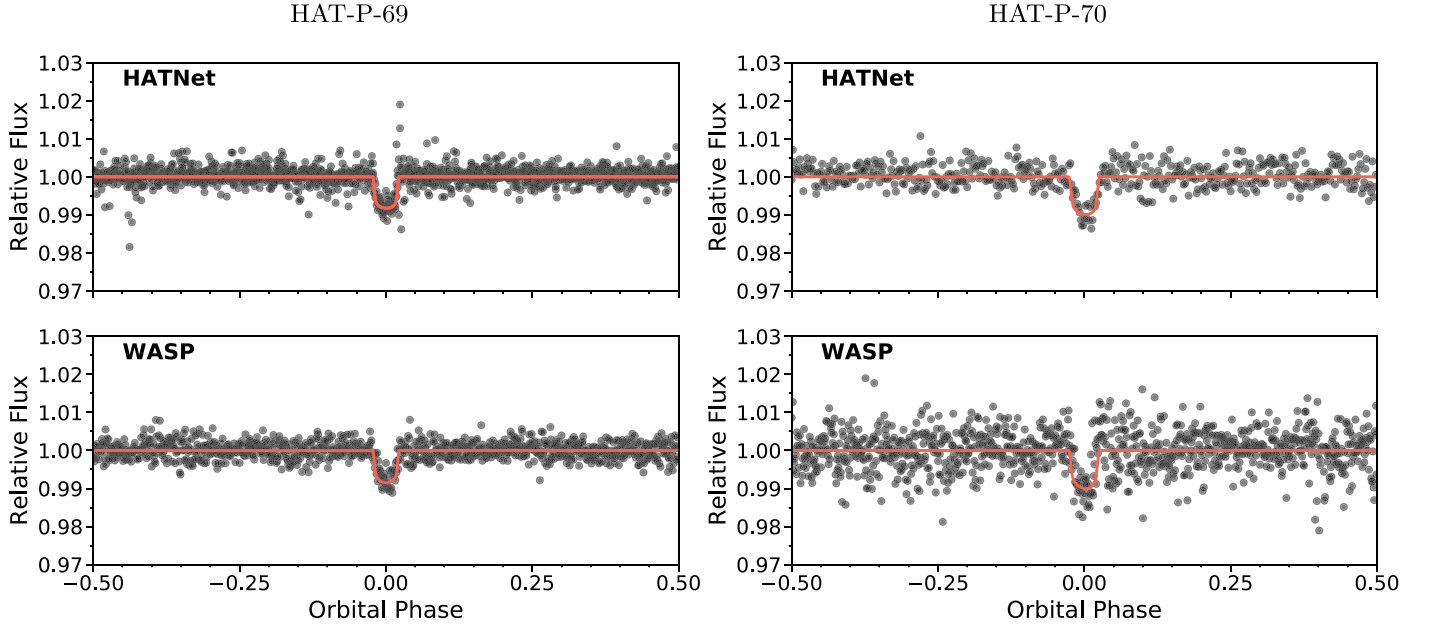


Figure 1. Discovery light curves of HAT-P-69 (left) and HAT-P-70 (right). The light curves have been averaged in phase with bins of width 0.002. The top panels show the HATNet light curves, and the bottom panels show the WASP light curves.

Table 1
Summary of Photometric Observations

Target	Facility	Date(s)	Number of Images ^a	Cadence (s) ^b	Filter
HAT-P-69	WASP-South/North	2009 Jan 14–2012 Apr 23	25282	432	WASP Broadband
HAT-P-69	HAT-6	2010 Nov 2–2011 Apr 21	10384	229	<i>r</i>
HAT-P-69	HAT-7	2010 Nov 2–2011 May 25	8707	233	<i>r</i>
HAT-P-69	HAT-7	2011 Feb 14–2011 Jun 3	4539	215	<i>r</i>
HAT-P-69	KeplerCam 1.2 m	2011 Dec 15	93	170	<i>z</i>
HAT-P-69	KeplerCam 1.2 m	2012 Jan 3	417	44	<i>z</i>
HAT-P-69	LCO BOS 1.0 m	2012 Feb 20	170	48	<i>i</i>
HAT-P-69	LCO BOS 1.0 m	2012 Apr 8	223	68	<i>i</i>
HAT-P-69	KeplerCam 1.2 m	2013 Mar 14	617	24	<i>i</i>
HAT-P-69	KeplerCam 1.2 m	2018 Feb 6	759	22	<i>z</i>
HAT-P-69	KeplerCam 1.2 m	2018 Mar 2	886	22	<i>z</i>
HAT-P-69	TRAPPIST 0.6 m	2018 Nov 11	234	60	RC ^c
HAT-P-69	TRAPPIST 0.6 m	2018 Dec 5	251	60	GC ^d
HAT-P-69	KeplerCam 1.2 m	2019 Jan 12	381	18	<i>i</i>
HAT-P-69	TRAPPIST 0.6 m	2019 Feb 9	223	52	RC
HAT-P-69	<i>TESS</i>	2019 Jan 8–2019 Feb 1	1087	1800	<i>TESS</i>
HAT-P-70	WASP-North	2008 Oct 13–2011 Feb 4	19266	351	WASP Broadband
HAT-P-70	HAT-9	2009 Sep 19–2010 Mar 30	9987	224	<i>r</i>
HAT-P-70	TRAPPIST 0.6 m	2018 Sep 23	238	40	RC
HAT-P-70	TRAPPIST 0.6 m	2018 Nov 5	376	40	RC
HAT-P-70	TRAPPIST 0.6 m	2018 Nov 27	231	35	RC
HAT-P-70	TRAPPIST 0.6 m	2018 Dec 9	209	42	GC
HAT-P-70	<i>TESS</i>	2018 Nov 15–2018 Dec 10	1024	1800	<i>TESS</i>
HAT-P-70	KeplerCam 1.2 m	2019 Feb 21	563	18	<i>i</i>

Notes.

^a Outlying exposures have been discarded.

^b Median time difference between points in the light curve. Uniform sampling was not possible due to visibility, weather, and pauses.

^c RC: Red continuum filter centered at 7128 Å with width of 58 Å.

^d GC: Green continuum filter centered at 5260 Å with width of 65 Å.

signal. We include secondary eclipse signals halfway between transits, with a depth parameterized by f_p , the relative brightness of the planet’s dayside hemisphere.

Since we are interested in temporal signals in the out-of-eclipse light curve, we do not use the detrended time series and

instead multiply the phase curve model by generalized polynomials in time to capture all nonastrophysical time-dependent signals in the raw light curve, which are likely attributable to instrumental systematics. The raw light curves shown in Figures 3 and 4 display clear long-term temporal

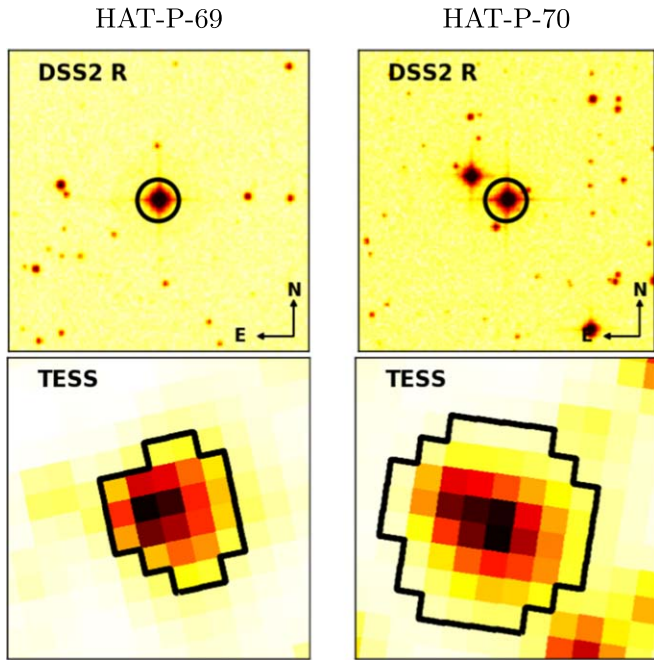


Figure 2. Fields surrounding each of the planet-hosting stars. Top: $4' \times 4'$ Digitized Sky Survey *R* cutouts of HAT-P-69 and HAT-P-70. Bottom: *TESS* Full Frame Image cutouts of HAT-P-69 and HAT-P-70. The DSS and *TESS* cutouts are plotted at the same scale and orientation. The photometric apertures used to extract the *TESS* light curves are marked.

trends, as well as discontinuities in flux that occur during momentum dumps.

Given these discontinuities, we split each light curve into small segments separated by momentum dumps and fit a separate polynomial systematics model to each segment. The orders of the polynomials used in the final fit are determined by first fitting each segment individually and minimizing the Bayesian information criterion (BIC), defined as $\text{BIC} = \chi^2 + k \ln(n)$, where k is the number of fitted parameters, and n is the number of data points. After optimizing the polynomial orders, we carry out a joint fit of the full light curve.

For HAT-P-70, we find that the nonastrophysical systematics in the segments are well described by polynomials of second to third order. In the joint fit, we report a marginal 2.4σ secondary eclipse detection of 159 ± 65 ppm, while the atmospheric brightness modulation amplitude is consistent with zero. Figure 4 shows the systematics-corrected and phase-folded light curve in the vicinity of the secondary eclipse, along with the best-fit model.

To evaluate the statistical significance of this HAT-P-70 b secondary eclipse detection, we compare the BIC of a joint fit that includes only transits and secondary eclipses (fixing B_1 to zero) with the BIC of a fit that assumes a flat out-of-transit light curve (fixing B_1 and f_p to zero). The difference in BIC is less than 0.1, indicating that the secondary eclipse detection is not formally statistically robust. From an analogous analysis of the HAT-P-69 phase curve, we do not detect any significant secondary eclipse depth or phase curve signal.

2.1.3. Independent Identification by WASP

HAT-P-69 and HAT-P-70 were both independently identified as planet candidates by the WASP survey (Schanche et al. 2019). The northern facility (SuperWASP-North) and the

southern facility (WASP-South) both consist of arrays of eight 200 mm $f/1.8$ Canon telephoto lenses on a common mount. Each camera is coupled with $2K \times 2K$ detectors, yielding a field of view of 7.8×7.8 per camera (Pollacco et al. 2006). HAT-P-69 was observed by both WASP-South and SuperWASP-North, producing 25,200 photometric points spanning from 2009 January 14 to 2012 April 23. HAT-P-70 was observed by SuperWASP-North, producing 19,200 observations spanning 2008 October 13 to 2011 February 4. These long baseline observations are plotted in Figure 1 and were included in the global modeling (Section 3.2) to help refine the transit ephemeris.

2.1.4. Ground-based Follow-up Observations

A series of facilities provided follow-up photometry of HAT-P-69 and HAT-P-70 to confirm the transit signal, improve the determination of the planet radius, and increase the precision of the transit ephemeris. A number of transit observations were obtained with the FLWO 1.2 m telescope and KeplerCam, a $4K \times 4K$ CCD camera operated with 2×2 binning, giving a plate scale of $0''.672 \text{ pixel}^{-1}$. Photometry was extracted as per Bakos et al. (2010). Follow-up photometry was also obtained using the Las Cumbres Observatory (LCO; Brown et al. 2013) network. These observations included transits obtained via the 0.8 m LCO telescope located at the Byrne Observatory at Sedgwick, California, using the SBIG STX-16803 $4K \times 4K$ camera with a field of view of $16' \times 16'$. Observations were also obtained using the 1 m LCO telescope at Siding Spring Observatory, Australia, using the Sinistro Fairchild CCD, with a field of view of $27' \times 27'$ over the $4K \times 4K$ detector. Additional photometric follow-up was obtained using the TRAPPIST (TRANSiting Planets and Planetesimals Small Telescope) North facility (Jehin et al. 2011; Gillon et al. 2013; Barkaoui et al. 2019) at Oukaïmeden Observatory in Morocco. TRAPPIST-North is a 0.6 m robotic photometer employing a $2K \times 2K$ CCD with a field of view of 19.8×19.8 at a plate scale of $0''.6$ per pixel.

The dates, cadences, and filters used in these observations are summarized in Table 1. The light curves are made available in Tables 2 and 3 and shown in Figures 5 and 6.

2.2. Spectroscopy

We carried out a series of spectroscopic follow-up observations to confirm the nature of the transiting candidates, constrain the masses, and measure the orbital obliquities of the companions. The observations are listed in Table 4 and summarized below.

The Tillinghast Reflector Echelle Spectrograph (TRES; Fűrész 2008) on the 1.5 m telescope at FLWO, Arizona, was used to obtain dozens of spectra for each system. TRES is a fiber-fed echelle spectrograph with a spectral resolution of $R = 44,000$ over the wavelength region of 3850–9100 Å. The observing strategy and data reduction process are described by Buchhave et al. (2012). Each spectrum is measured from the combination of three consecutive observations for optimal cosmic-ray rejection, and the wavelength solution is provided by bracketing ThAr hollow cathode lamp exposures. A series of TRES spectra were obtained at phase quadratures to most efficiently constrain the mass of the planets. For HAT-P-69, relative radial velocities were obtained using a multiorder analysis (Quinn et al. 2012) of the TRES spectra. For HAT-P-70,

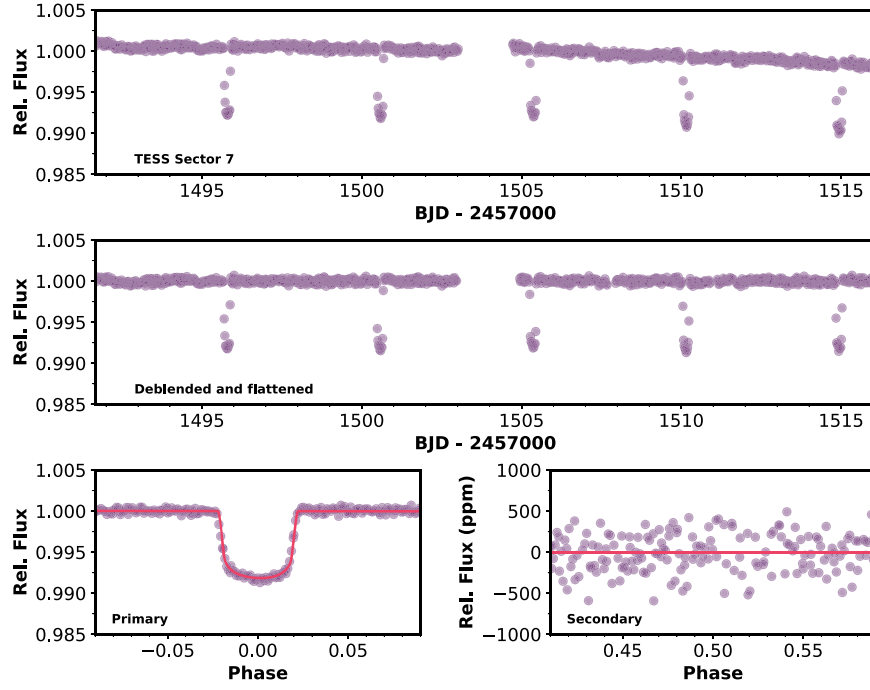


Figure 3. *TESS* light curve of HAT-P-69. Top: raw *TESS* light curve. Center: detrended light curve. Lower left: detrended light curve phase-folded to the transit ephemeris, showing the transit and associated best-fit model (plotted in red). Lower right: detrended light curve in the region of the secondary eclipse, assuming a circular orbit.

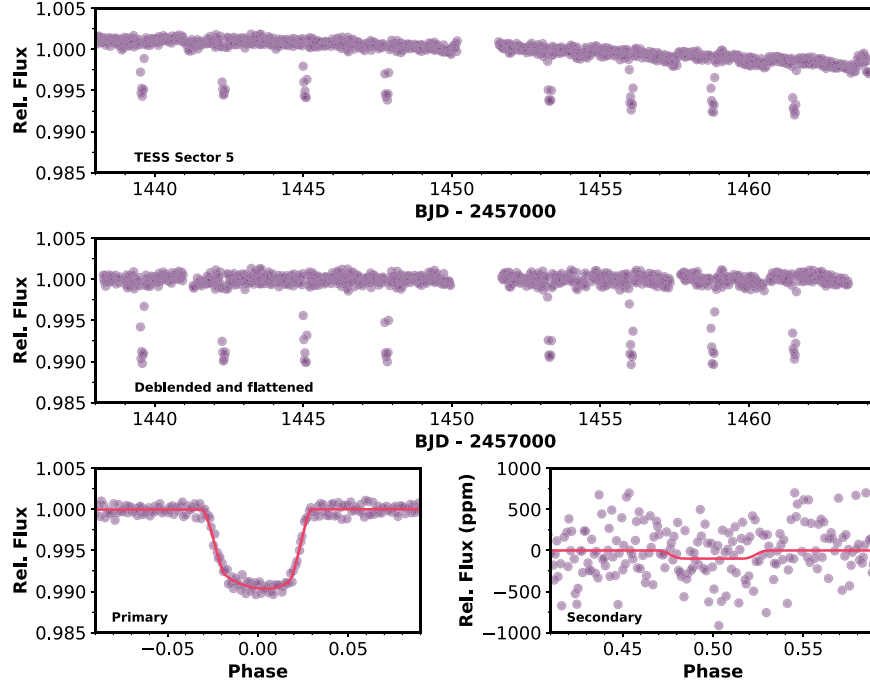


Figure 4. *TESS* light curve of HAT-P-70. Panel contents as described in Figure 3. The tentative detection of a secondary eclipse with a depth of 159 ± 65 ppm is shown in the lower right panel. The best-fit model is shown in red.

we modeled the stellar line profiles derived from a least-squares deconvolution (LSD; Donati et al. 1997) to derive the absolute radial velocities of each spectrum. In our experience with rapidly rotating stars, the best radial velocities are obtained by modeling of the LSD-derived line profiles. The TRES velocities for HAT-P-69 and HAT-P-70 are listed in Tables 5 and 6 and plotted in Figures 7 and 8, respectively.

Spectroscopic observations were also obtained with TRES throughout the transits of each planet. These observations allow us to measure variations in the stellar line profile due to the partial obscuration of the photosphere of the rapidly rotating star (Collier Cameron et al. 2010). By measuring the planetary “shadow” on the line profile of the star, we confirm that the photometric transit signal is indeed caused by a small body that

Table 2
Differential Photometry of HAT-P-69

BJD	Mag (Raw) ^a	Mag (EPD)	Mag (TFA)	σ Mag	Instrument	Filter
2455502.9688207	9.12413	10.01248	10.00835	0.00161	HATNet	r'
2455502.9733846	9.11519	10.0089	10.00331	0.0016	HATNet	r'
2455502.9776452	9.11541	10.01343	10.00835	0.0016	HATNet	r'
2455502.9819047	9.12139	10.01393	10.01161	0.0016	HATNet	r'
2455502.9862569	9.10128	10.00651	9.99933	0.00159	HATNet	r'

Note.

^a Raw, EPD, and TFA magnitudes are presented for HATNet light curves. The detrending and potential blending may cause the HATNet transit to be shallower than the true transit in the EPD and TFA light curves. This is accounted for in the global modeling by the inclusion of a dilution factor. Follow-up light curves have been treated with EPD simultaneous to the transit fitting. Pre-EPD magnitudes are presented for the follow-up light curves.

(This table is available in its entirety in machine-readable form.)

Table 3
Differential Photometry of HAT-P-70

BJD	Mag (Raw) ^a	Mag (EPD)	Mag (TFA)	σ Mag	Instrument	Filter
2455093.9914136	8.8238	9.69444	9.69370	0.00177	HATNet	r'
2455093.9939800	8.83789	9.69611	9.70024	0.00179	HATNet	r'
2455093.9966693	8.84903	9.67121	9.67967	0.0018	HATNet	r'
2455093.9993076	8.80637	9.70271	9.69896	0.00177	HATNet	r'
2455094.0019585	8.84992	9.69871	9.69148	0.00181	HATNet	r'

Note.

^a Raw, EPD, and TFA magnitudes are presented for HATNet light curves. The detrending and potential blending may cause the HATNet transit to be shallower than the true transit in the EPD and TFA light curves. This is accounted for in the global modeling by the inclusion of a dilution factor. Follow-up light curves have been treated with EPD simultaneous to the transit fitting. Pre-EPD magnitudes are presented for the follow-up light curves.

(This table is available in its entirety in machine-readable form.)

is transiting the bright, rapidly rotating target star, as opposed to being the diluted signal of a much fainter eclipsing binary that is spatially blended with the target star in the photometric aperture. The observing strategy and analysis largely follow the procedure laid out by Zhou et al. (2016). We observed three partial transits of HAT-P-69 on 2017 March 8 and 13 and 2019 January 12, with the Doppler shadow of the planet clearly detected in each individual transit (Figure 9). Two partial transits of HAT-P-70 were obtained on 2019 February 21 and March 4. Observations on 2019 February 21 were hampered by poor weather, but the subsequent transit on 2019 March 4 clearly revealed the planet shadow (Figure 10). These observations are used in the global analysis (Section 3.2) to derive the projected spin-orbit angle of the systems.

One additional partial transit of HAT-P-69 b was obtained via the High Resolution Spectrograph (HRS; Crause et al. 2014) on the Southern African Large Telescope (SALT). HRS is a fiber-fed echelle spectrograph used in the medium resolution mode, yielding a spectral resolution of $R = 40,000$ over the wavelength region of 3700–5500 Å over the blue arm of the spectrograph. Observations from the red arm of the spectrograph were not used due to the fewer line counts over its spectral coverage. The observations were obtained covering the ingress of HAT-P-69 b on 2015 March 6, covering 11 spectra with integration times of 700 s each. The target star remained at an altitude of 47°–53° throughout the transit observations. The spectra were extracted and calibrated using the *MIDAS* pipeline (Kniazhev et al. 2016, 2017). The spectral line profiles were extracted via a process similar to that described above. The average line profile is subtracted, leaving a significant detection of the planetary transit over ingress (Figure 9).

In addition, a number of spectroscopic resources contributed to the initial spectroscopic vetting of the targets. Observations of HAT-P-69 were obtained using the High Resolution Echelle Spectrometer on the 10 m Keck I at Maunakea Observatory. Observations were also obtained using the High Dispersion Spectrograph on the 8.2 m Subaru telescope on Maunakea Observatory. In both cases, observations were made using the iodine cell, but did not yield high-precision velocities due to the rapid rotation of the star. They were not included in the analysis. We also made use of the CHIRON instrument on the SMARTS 1.5 m telescope at Cerro Tololo Inter-American Observatory (CTIO), Chile (Tokovinin et al. 2013), obtaining four observations of HAT-P-70. Similarly, reconnaissance observations were obtained with the SOPHIE echelle facility on the 1.93 m Haute-Provence Observatory, France, as well as the CORALIE spectrograph on the 1.2 m Euler telescope at the ESO La Silla Observatory, Chile. Given that the TRES observations vastly outnumber these reconnaissance observations, we incorporate only the TRES data in our global modeling.

3. Analysis

3.1. Properties of the Host Star

Both HAT-P-69 and HAT-P-70 are classified as rapidly rotating A stars based on their Two Micron All Sky Survey (2MASS; Skrutskie et al. 2006) $J - K$ colors and the reconnaissance spectra from *TRES*. Rapidly rotating stars have spectral lines that are blended and unresolved, making standard spectral classifications more difficult. In addition, the gravity-darkening effect causes the derived atmospheric parameters,

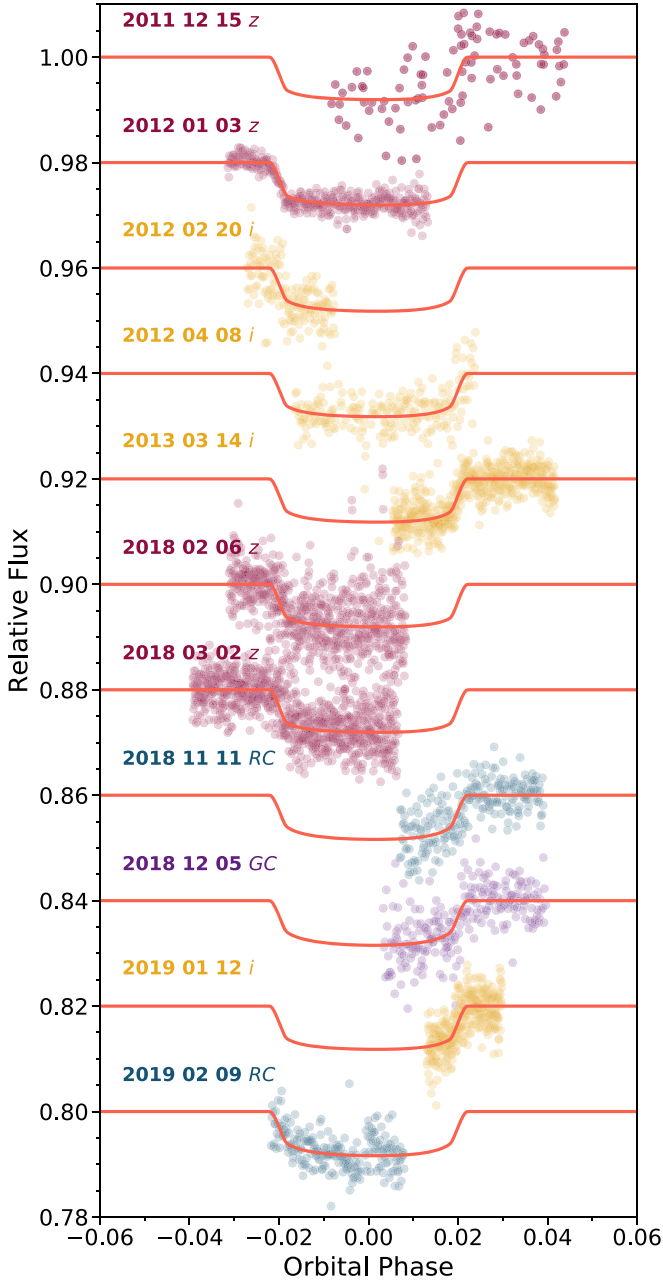


Figure 5. Ground-based follow-up light curves for HAT-P-69, vertically separated for clarity. The photometric bandpass and date of the observations are labeled. The facilities contributing to each light curve are presented in Table 1.

such as effective temperature, to be dependent on our viewing angle. The same star would appear hotter when viewed pole-on and cooler when viewed along the equator. We adopt the approach described in Zhou et al. (2019) and match the spectral energy distribution (SED) of the star against a grid of synthetic magnitudes computed from the Geneva 2D rotational isochrones (Ekström et al. 2012) for a range of inclination angles. This is performed as part of the global modeling described in Section 3.2, as the transit light curve also contributes to constraining the inclination angle of the system.

The SEDs for both stars are shown in Figures 11 and 12. We find that both stars are late A dwarfs. HAT-P-69 has a mass of $1.648^{+0.058}_{-0.026} M_{\odot}$, radius of $1.926^{+0.060}_{-0.031} R_{\odot}$, and effective temperature of 7394^{+360}_{-600} K. HAT-P-70 has a mass of $1.890^{+0.010}_{-0.013} M_{\odot}$,

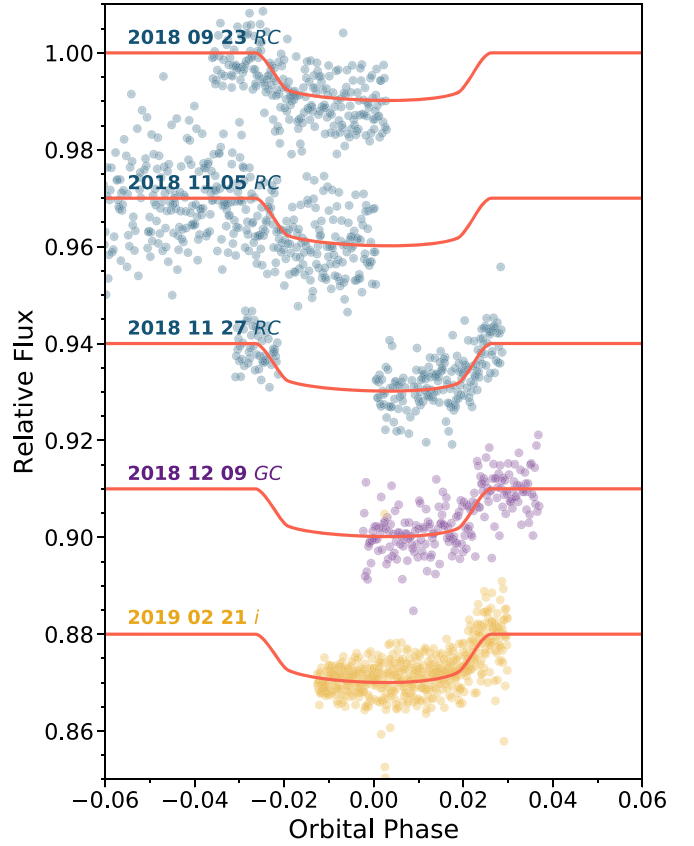


Figure 6. Ground-based follow-up light curves for HAT-P-70; description as in Figure 5.

radius of $1.858^{+0.119}_{-0.091} R_{\odot}$, and effective temperature of 8450^{+540}_{-690} K.

We check this rotational SED analysis with an independent fit of the SEDs to Kurucz atmosphere models of nonrotating stars (Kurucz 1992). We find HAT-P-69 to have $T_{\text{eff}} = 7650 \pm 400$ K, $R_{\star} = 1.88 \pm 0.19 R_{\odot}$, and reddening of $A(v) = 0.01 \pm 0.01$. HAT-P-70 has $T_{\text{eff}} = 8400 \pm 400$ K, $R_{\star} = 2.08 \pm 0.20 R_{\odot}$, with reddening of $A(v) = 0.30^{+0.01}_{-0.08}$. For both stars, the nonrotational SED analysis agrees well with that from the global modeling detailed above.

As a check on the determination of the stellar parameters, we independently derived the effective temperature and metallicity of each star using the *TRES* spectra and the Stellar Parameter Classification pipeline (Buchhave et al. 2010). We find HAT-P-69 to have $T_{\text{eff}} = 7557 \pm 52$ K and $[m/H] = +0.05 \pm 0.08$ dex, while HAT-P-70 has atmospheric parameters of $T_{\text{eff}} = 8246 \pm 93$ K and $[m/H] = -0.06 \pm 0.09$ dex. The spectroscopic stellar parameters agree to within 1σ with those measured from the SED, though the uncertainties are likely underestimated. The rapid rotation of the star causes difficulties in continuum normalization of the spectra, making accurate spectroscopic determination of the stellar parameters and associated uncertainties more difficult. We incorporate the metallicity measurements from spectra as Gaussian priors in the global modeling. For a more accurate understanding of stellar properties, we simultaneously fit the SED with the transit and rotational stellar isochrones in our global modeling, instead of relying on the spectra-derived values.

An accurate measurement of the projected stellar rotation rate is crucial for interpreting the Doppler transit data,

Table 4
Summary of Spectroscopic Observations

Target	Telescope/Instrument	Date Range	Number of Observations	Resolution	Observing Mode
HAT-P-69	FLWO 1.5 m TRES	2011 Oct 10–2017 Mar 14	45	44000	RV
HAT-P-69	SALT HRS	2015 Mar 6	11	40000	Transit
HAT-P-69	FLWO 1.5 m TRES	2017 Mar 8	18	44000	Transit
HAT-P-69	FLWO 1.5 m TRES	2017 Mar 13	17	44000	Transit
HAT-P-69	FLWO 1.5 m TRES	2019 Jan 12	22	44000	Transit
HAT-P-70	FLWO 1.5 m TRES	2013 Feb 1–2019 Feb 20	43	44000	RV
HAT-P-70	FLWO 1.5 m TRES	2019 Feb 21	19	44000	Transit
HAT-P-70	FLWO 1.5 m TRES	2019 Mar 4	19	44000	Transit

constraining the stellar gravity-darkening effect, and constraining the stellar oblateness. To measure the projected rotation velocity, we model the LSD spectral line profiles using a kernel that incorporates the effects of stellar rotation and radial-tangential macroturbulence via a numerical disk integration, and we model the instrument line broadening as a Gaussian convolution. We find HAT-P-69 to have $v \sin I_* = 77.40 \pm 0.60 \text{ km s}^{-1}$ and a macroturbulent velocity of $v_{\text{mac}} = 5.6 \pm 4.2 \text{ km s}^{-1}$. For HAT-P-70, the results are $v \sin I_* = 99.87 \pm 0.65 \text{ km s}^{-1}$ and $v_{\text{mac}} = 4.77 \pm 0.86 \text{ km s}^{-1}$.

3.2. Global Modeling of System Parameters

We perform a global analysis of the systems to model the large suite of observations available for HAT-P-69 and HAT-P-70. This global model simultaneously incorporates the photometric transit, radial velocities, stellar parameter constraints, Doppler transits, and the effect of photometric gravity darkening on the transit light curve and observed stellar properties.

Our modeling process largely follows that described by Zhou et al. (2019). Rapid rotation distorts the shapes of stars; they become oblate along the equator, causing the poles to be hotter and brighter, while the equator becomes cooler and darker (von Zeipel 1924). This gravity-darkening effect causes both the transit light curve (Barnes 2009) and the observed SED of the star (Brandt & Huang 2015) to depend on the viewing direction. The photometric transit is modeled using the *simuTrans* package from Herman et al. (2018), which accounts for both the gravity-darkened nonuniform brightness distribution of the stellar disk and the ellipsoidal nature of the rapidly rotating star. The stellar properties are inferred from the Geneva 2D rotational isochrones (Ekström et al. 2012), which incorporate the effects of rotation on stellar evolution and include prescriptions for the oblateness of the stars based on their rotation rates. In the case of an oblique transiting geometry about gravity-darkened stars, the resulting light curve often exhibits asymmetry because of the latitude dependence of the surface brightness distribution. This effect is detected for HAT-P-70 b and explored in greater depth in Section 3.4.

The limb-darkening coefficients are interpolated from the values of Claret & Bloemen (2011) and Claret (2017) for the Sloan and *TESS* bands. They are constrained by a Gaussian prior of width 0.02 during the global modeling, representing the difference in the limb-darkening coefficients should the stellar parameters be different by 1σ . To model the transit light curves, we adopt a gravity-darkening coefficient β from interferometric observations of Vega ($\beta = 0.231 \pm 0.028$;

Monnier et al. 2012). Similar interferometric gravity-darkening coefficients have been measured for other rapidly rotating A stars (e.g., $\alpha \text{ Cep } \beta = 0.216 \pm 0.021$; Zhao et al. 2009). To account for the uncertainty in the gravity-darkening coefficient, it is modeled in the global fit as a free parameter constrained about the value and uncertainty of Vega reported in Monnier et al. (2012). The model fitting procedure also includes detrending of the ground-based follow-up light curves, via a linear combination of effects, including the pixel position of the target star, air mass, and background count values. We account for the 30 minute cadence of the *TESS* by supersampling and integrating the model over the exposure time.

The stellar parameters are constrained by the SED of the stars over the Tycho-2 (Høg et al. 2000), APASS (Henden et al. 2016), and 2MASS (Skrutskie et al. 2006) photometric bands, as well as the parallax from *Gaia* data release 2 (Gaia Collaboration et al. 2018). Local reddening is constrained by the maximum reddening value from the dust maps of Schlafly & Finkbeiner (2011), assuming $A_V = 3.1E(B - V)$. To account for the uncertainties in our deblending of the *TESS* light curves, we also include a *TESS* light curve dilution parameter, closely constrained by a Gaussian prior, with width derived from the reported uncertainties in the *TESS* band magnitudes of the target and nearby stars from TIC v6.

The Doppler transit signal is simultaneously modeled with the light curve and provides the best constraint on the projected spin-orbit angle λ for the orbital plane of the planets. We model variations of the stellar line profiles via a 2D integration of the rotating stellar surface being occulted by the transiting planet, incorporating the effects of differential limb darkening, radial-tangential macroturbulence, and instrument broadening.

To derive the best-fit system parameters and their associated uncertainties, we perform a Markov chain Monte Carlo analysis using the *emcee* package (Foreman-Mackey et al. 2013). The resulting stellar and planetary parameters are shown in Tables 7 and 8, respectively.

3.3. Blending and Astrophysical False-positive Scenarios

Many astrophysical scenarios can mimic the transit signal of a planetary system. False-positive scenarios such as M dwarf companions with radii similar to substellar counterparts are ruled out by the mass constraints imposed by our radial velocity measurements. The possibility that the transit signals are due to fainter eclipsing binaries whose eclipses are diluted by the brighter target stars is more difficult to eliminate. We adopt a number of observations, including diffraction-limited imaging and analysis of the spectroscopic transit, to eliminate this possibility.

Table 5
Relative Radial Velocities of HAT-P-69

BJD (UTC)	Relative RV ^a (km s ⁻¹)	σ RV (km s ⁻¹)	Instrument
2455844.990516	1.437	0.433	TRES
2455889.044893	0.782	0.159	TRES
2455904.899944	0.763	0.200	TRES
2456399.650041	0.328	0.178	TRES
2456400.656614	0.462	0.151	TRES
2456403.681071	0.389	0.121	TRES
2456404.671615	0.138	0.134	TRES
2456409.670360	0.171	0.142	TRES
2456410.671948	0.293	0.140	TRES
2457819.604459	0.619	0.175	TRES
2457819.616148	0.473	0.155	TRES
2457819.627797	0.851	0.150	TRES
2457819.639439	0.482	0.121	TRES
2457819.651291	0.487	0.172	TRES
2457819.663107	0.587	0.135	TRES
2457819.675045	0.781	0.118	TRES
2457819.686914	0.753	0.125	TRES
2457819.698568	0.684	0.119	TRES
2457819.710512	0.728	0.107	TRES
2457819.723092	0.690	0.140	TRES
2457819.734747	0.487	0.129	TRES
2457819.746511	0.667	0.098	TRES
2457819.758189	0.733	0.134	TRES
2457819.770017	0.577	0.161	TRES
2457819.781718	0.593	0.122	TRES
2457819.793343	0.640	0.120	TRES
2457819.804946	0.364	0.152	TRES
2457819.816560	0.805	0.178	TRES
2457819.828173	0.847	0.156	TRES
2457820.675448	0.460	0.110	TRES
2457820.687137	0.732	0.099	TRES
2457820.698797	0.384	0.148	TRES
2457820.710475	0.553	0.148	TRES
2457820.722152	0.711	0.123	TRES
2457825.760728	0.264	0.123	TRES
2457825.772683	0.466	0.162	TRES
2457825.784297	0.350	0.146	TRES
2457825.795980	0.518	0.147	TRES
2457826.645765	0.480	0.157	TRES
2457826.657442	0.242	0.165	TRES
2457826.669091	0.062	0.161	TRES
2457826.682487	0.199	0.176	TRES
2457826.694234	0.194	0.110	TRES
2457826.705923	0.373	0.136	TRES
2457826.717589	0.292	0.225	TRES
2457826.729296	0.255	0.151	TRES
2457826.741008	0.199	0.103	TRES
2458495.942762	0.618	0.228	TRES
2458495.954736	0.642	0.330	TRES
2458495.966877	0.938	0.285	TRES
2458495.979216	0.286	0.303	TRES
2458495.991201	0.566	0.356	TRES
2458496.003036	0.810	0.192	TRES

Note.

^a Relative radial velocities from a multiorder cross correlation. Internal errors excluding the component of astrophysical/instrumental jitter considered in Section 3. Velocities exclude those taken in transit.

To rule out spatially nearby companions, we obtained observations with the NN-explore Exoplanet Stellar Speckle Imager (NESSI; Scott et al. 2018) on the 3.5 m WIYN telescope at Kitt Peak National Observatory, Arizona. Speckle

Table 6
Relative Radial Velocities of HAT-P-70

BJD (UTC)	RV ^a (km s ⁻¹)	σ RV (km s ⁻¹)	Instrument
2456324.697671	24.350	0.642	TRES
2456342.685872	24.867	0.616	TRES
2457671.822407	25.153	0.708	TRES
2457671.830590	25.270	0.620	TRES
2457671.838751	26.999	0.532	TRES
2457671.846928	25.516	0.639	TRES
2457671.855187	25.525	0.727	TRES
2457671.863348	25.804	1.043	TRES
2457671.871531	25.827	0.599	TRES
2457671.880432	26.936	0.676	TRES
2457671.892204	24.786	1.114	TRES
2457671.900399	24.601	0.688	TRES
2457671.908554	24.334	0.934	TRES
2457671.917565	24.760	0.634	TRES
2457671.925743	25.362	0.773	TRES
2457671.933920	24.981	0.663	TRES
2457671.942121	25.324	0.659	TRES
2457671.950363	26.011	0.538	TRES
2457671.958645	25.100	0.825	TRES
2457671.966979	25.709	0.726	TRES
2457671.975226	24.904	0.592	TRES
2457671.983427	25.817	0.819	TRES
2457671.991639	24.845	0.677	TRES
2457672.000309	25.261	0.536	TRES
2457672.008573	24.851	0.584	TRES
2457672.016844	25.661	0.839	TRES
2457672.025149	25.769	0.434	TRES
2458527.601110	25.803	1.160	TRES
2458531.776169	25.321	1.741	TRES
2458532.755301	24.806	0.962	TRES
2458534.591655	24.475	0.630	TRES
2458534.599808	25.870	0.654	TRES
2458534.607915	25.156	1.032	TRES
2458534.616045	24.988	0.569	TRES
2458534.624158	25.590	0.992	TRES
2458534.632322	24.981	0.916	TRES
2458534.640470	26.307	1.199	TRES
2458534.648681	24.680	0.628	TRES
2458534.656811	25.248	1.155	TRES
2458534.664964	24.315	0.761	TRES
2458534.673094	25.971	0.920	TRES
2458534.681230	24.672	0.470	TRES
2458534.689354	24.547	0.848	TRES
2458535.714170	24.300	0.508	TRES
2458535.722375	23.870	0.994	TRES
2458535.730499	24.905	2.141	TRES
2458535.738629	23.029	3.309	TRES
2458546.689854	25.441	0.382	TRES
2458546.698076	26.287	0.618	TRES
2458546.706287	24.819	0.922	TRES
2458546.714516	26.252	0.741	TRES
2458546.722686	23.979	0.821	TRES
2458546.730914	25.292	1.133	TRES
2458546.739183	25.804	1.377	TRES

Note.

^a Absolute velocities derived from the least-squares deconvolution profiles. Internal errors excluding the component of astrophysical/instrumental jitter considered in Section 3. Velocities exclude those taken in transit.

imaging gives a resolution of $\gtrsim 0''.04$ in both the r -narrow and z -narrow bands for both HAT-P-69 and HAT-P-70, corresponding to spatial scales as close to the stars as 14–22 au (at

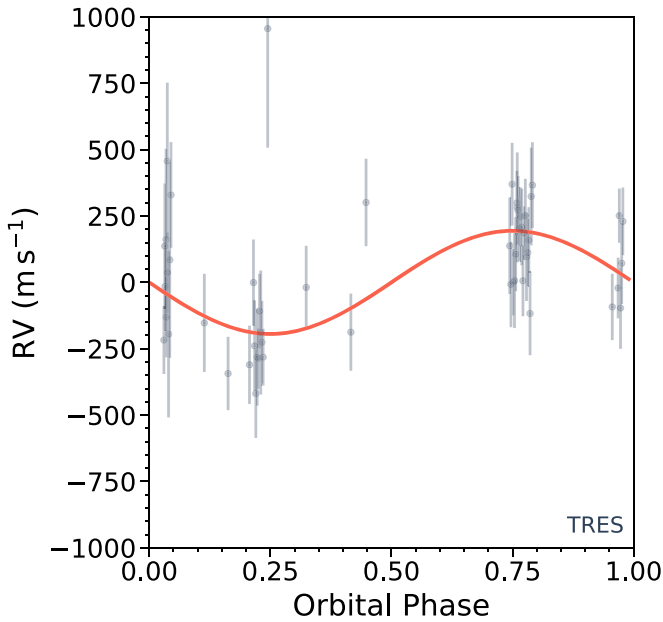


Figure 7. TRES radial velocities for HAT-P-69. The best-fit orbit from the global model is plotted in red. The fitted radial velocity jitter has been added to the per-point uncertainties in quadrature.

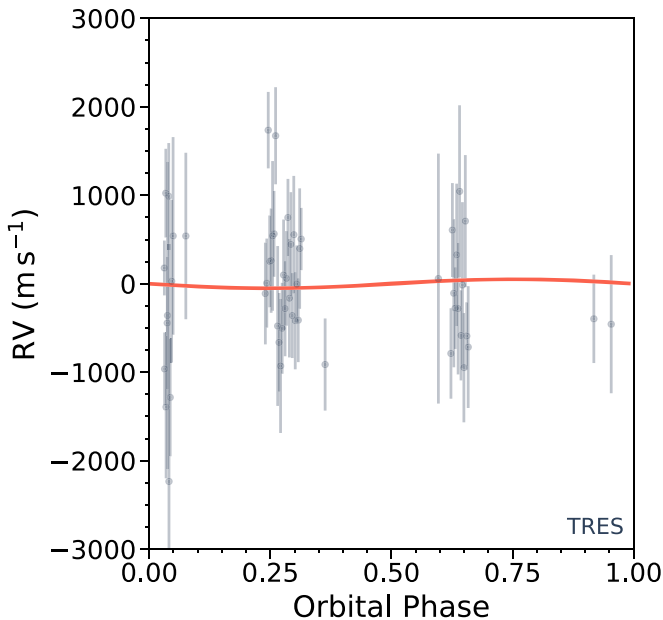


Figure 8. TRES radial velocities for HAT-P-70; description as in Figure 7.

562 nm and 832 nm, respectively). The corresponding constraints from NESSI are plotted in Figure 13. In addition, we obtained *J*- and *Ks*-band infrared seeing limited imaging HAT-P-69 with the WIYN High-Resolution Infrared Camera (WHIRC; Smee et al. 2011), also finding no visual companions to the target star.

Finally, the Doppler detection of the planetary transit confirms that the transits indeed occur around the rapidly rotating, bright A star hosts, not background stars (e.g., Collier Cameron et al. 2010). The depth of the spectroscopic shadow agrees with the depth observed in the photometric light curves, suggesting that the dilution due to background sources is negligible.

3.4. Detection of an Asymmetric Gravity-darkened Transit for HAT-P-70

A transiting planet crossing a gravity-darkened stellar disk may exhibit an asymmetric transit when the projected spin-orbit angle is misaligned with the stellar rotation axis. The effects specific to gravity darkening are only visible at the parts-per-thousand level, and as such they are difficult to detect with ground-based data. The only previous confirmed instance of asymmetric gravity darkening being observed for a planetary system is for Kepler-13. The asymmetric transit light curves of Kepler-13 were identified and modeled by Szabó et al. (2011), Barnes et al. (2011), and Herman et al. (2018). Subsequent ground-based Doppler transit confirmation of the spin-orbit misalignment was performed by Johnson et al. (2014) and an eventual joint light curve and spectroscopic transit model developed by Masuda (2015).

The *TESS* light curves of HAT-P-70 exhibit asymmetric transits similar to those seen for Kepler-13. The transit is shallower at ingress and deeper near egress, indicating that the planet traverses a stellar surface that is darker near ingress and brighter near egress. Our global model reproduces such a transit, with the projected spin-orbit misaligned at $21.2^{+4.6}_{-3.6}$ ° and the stellar pole inclined to the line of sight by $58.2^{+1.6}_{-1.2}$ ° degrees. Figure 14 shows the *TESS* transit light curve, with the best-fit standard and gravity-darkened transit models over-plotted. An asymmetry at the 500 ppm level can be seen in the residuals to the standard transit model, akin to that seen for Kepler-13.

We note that we make use of the bolometric gravity-darkening coefficient β in our light curve modeling. Improvements can be made via a more careful treatment for the band dependence of the gravity-darkening effect (e.g., Espinosa Lara & Rieutord 2011). We note, though, that running the global modeling while allowing β to be free reproduces the same projected obliquity λ value to within uncertainties, and as such the actual adopted gravity-darkening coefficient is not critical to the modeling.

4. Occurrence Rate of Hot Jupiters from *TESS*

Although hot Jupiters were some of the earliest exoplanets to be discovered, they are not intrinsically common. Radial velocity searches from the Keck, Lick, and Anglo Australia Telescope programs of 1330 FGK stars revealed a hot Jupiter occurrence rate of $1.2 \pm 0.2\%$ ($<15 M_{\text{Jup}}$, <0.1 au; Marcy et al. 2005), revised to $1.20 \pm 0.38\%$ ($>0.1 M_{\text{Jup}}$, $P < 10$ days) by Wright et al. (2012) using the California Planet Search sample. Cumming et al. (2008) found an occurrence rate of $1.5 \pm 0.6\%$ ($>0.3 M_{\text{Jup}}$, <0.1 au) using the Keck planet search sample. Using the HARPS and CORALIE samples, Mayor et al. (2011) found a hot Jupiter occurrence rate of $0.89 \pm 0.36\%$ ($>0.15 M_{\text{Jup}}$, <11 days).

These radial velocity occurrence rates are generally thought to be higher than those offered by the *Kepler* survey. Studies by Howard et al. (2012) and Fressin et al. (2013) of the early *Kepler* data found rates of $0.4 \pm 0.1\%$ and $0.43 \pm 0.05\%$ for hot Jupiters, respectively. Recent analyses with improved stellar properties from Petigura et al. (2018) found that $0.57^{+0.14}_{-0.12}\%$ of main-sequence FGK stars ($5.0 > \log g > 3.9$, $4200 < T_{\text{eff}} < 6500$ K) host hot Jupiters. The measured giant planet occurrence rate from the *CoRoT* mission is higher than that from *Kepler*, finding 21 giant planets ($R_p > 5 R_{\oplus}$) within

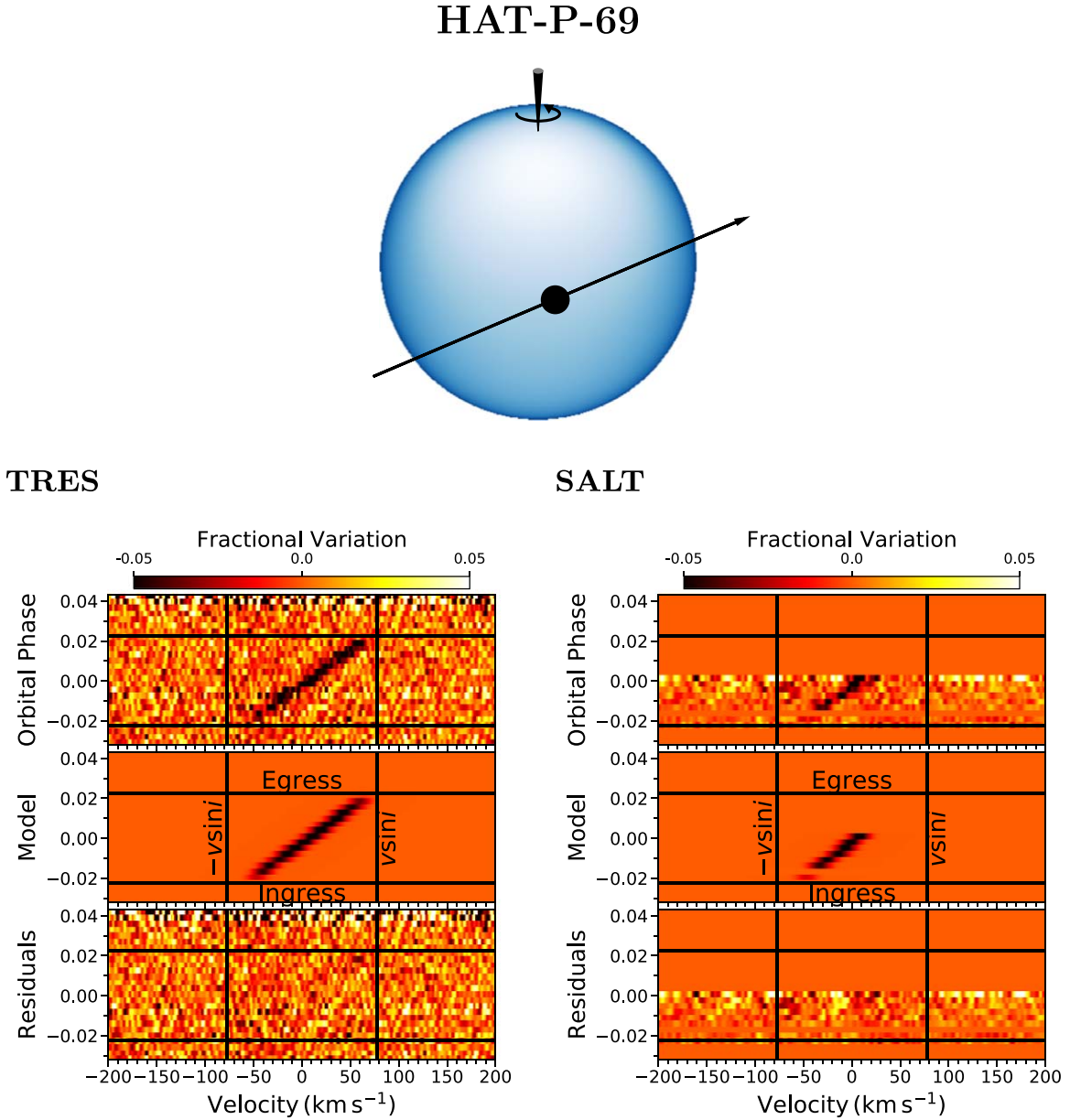


Figure 9. Doppler transits of HAT-P-69 b. Each Doppler map (top panel) shows the intensity of the line profile as a function of both velocity (relative to the line center) and orbital phase. The ingress and egress phases are marked with horizontal lines. The top segment shows the data from all of the observed transits, averaged into phase bins of size 0.003. The middle panel shows the best-fitting model, and the lower panel shows the residuals. A diagrammatic representation of the transit geometry of each system is shown at the top of the figure, with the relative sizes of the star and planet plotted to scale. The gravity-darkening effect is exaggerated to allow it to be easily seen. The left panel shows the Doppler transit signal for HAT-P-69 b, combined from three partial TRES transit observations. The right panel shows the partial transit of HAT-P-69 b via SALT HRS. Phases at which no data were obtained are colored in plain orange.

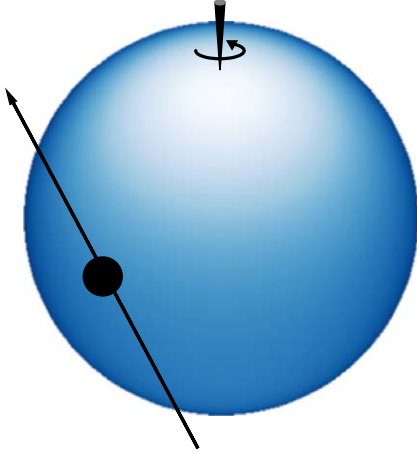
10 day period orbits, corresponding to an occurrence rate of $0.98 \pm 0.26\%$ (Deleuil et al. 2018).

The stars that host hot Jupiters are more metal-rich than random stars of the same spectral class (Santos et al. 2003; Valenti & Fischer 2005; Buchhave et al. 2012; Petigura et al. 2018). Differences between the metallicity distribution of the *Kepler* stellar sample and those of the radial velocity surveys have been raised as an explanation for the differences in the hot Jupiter occurrence rates (Wright et al. 2012), although Guo et al. (2017) showed that there is minimal difference between the *Kepler* field star metallicity distribution and that of the California Planet Search sample. Wang et al. (2015) offered a correction for the *Kepler* sample based on an improved classification of the subgiant population. They suggested that

multiplicity or a lower occurrence rate of hot Jupiters around subgiants may be the cause of the disagreement. Later, Bouma et al. (2018) showed that binarity is unlikely to be responsible for any disagreements between the Doppler and *Kepler* samples.

A radial velocity survey of intermediate-mass subgiants has shown that higher mass stars tend to host more gas giant planets within a few astronomical units (e.g., Johnson et al. 2010; Jones et al. 2014; Reffert et al. 2015; Ghezzi et al. 2018), though caveats regarding the accuracy of the mass measurements of these evolved stars should be noted (e.g., Lloyd 2013; Schlaufman & Winn 2013; Stello et al. 2017). The giant planets around subgiants tend to be found in orbits beyond 0.1 au; there appears to be a paucity of hot Jupiters around evolved stars.

HAT-P-70



TRES

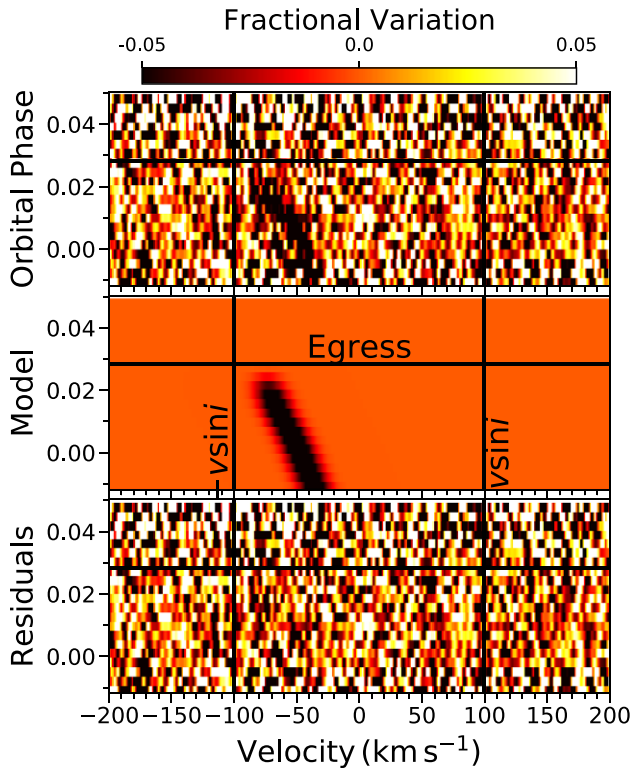


Figure 10. Doppler transit HAT-P-70 b as measured via two partial TRES transits. The figure follows the format specified in Figure 9.

These studies suggest that hot Jupiters undergo tidal orbital decay when a star begins evolving into a subgiant (Schlaufman & Winn 2013). The planets around these “retired A stars” tend to be in longer period and more circular orbits than those found around main-sequence stars (Jones et al. 2014), although recent discoveries have unveiled numerous hot Jupiters in close-in orbits about evolved stars (Grunblatt et al. 2018). These issues inspired us to look into the hot Jupiter occurrence rate around main-sequence A stars.

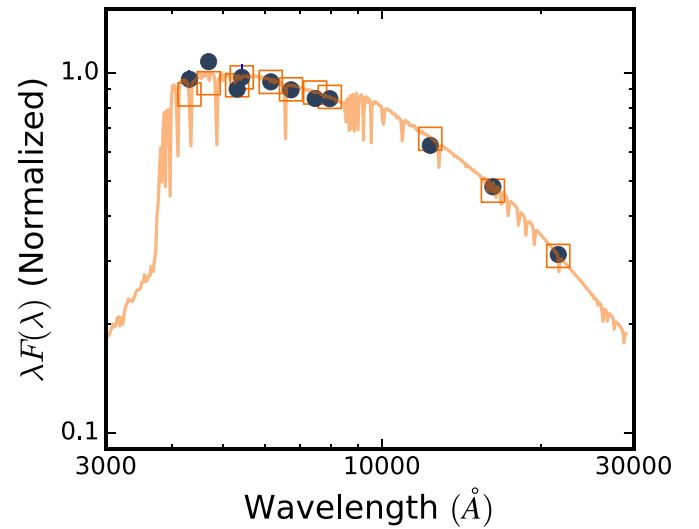


Figure 11. Spectral energy distribution of HAT-P-69 with the B , V , g' , r' , and i' bands from the AAVSO Photometric All-Sky Survey (APASS; Henden et al. 2016); G , B_P , and R_P from *Gaia* (Gaia Collaboration et al. 2018); and J , H , and K_s from 2MASS (Skrutskie et al. 2006). The synthetic spectrum is generated using ATLAS9 models (Castelli & Kurucz 2004) while accounting for the effect of the viewing geometry and gravity darkening of the host star.

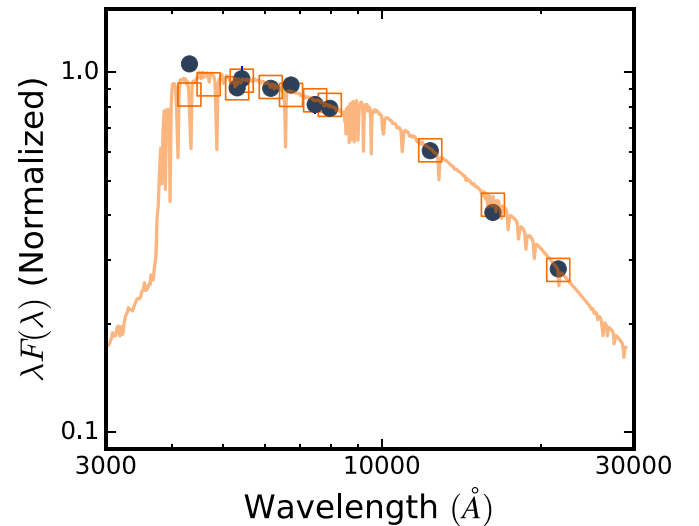


Figure 12. Spectral energy distribution of HAT-P-70, similar to Figure 11. See caption for Figure 11.

In this section, we aim to examine the hot Jupiter occurrence rate via the *TESS* stellar population, with two key differences from the previous works from *Kepler*:

1. The *TESS* stellar population encompasses bright stars covering one-quarter of the sky. This sample is a significantly closer (150 pc for a solar-type main-sequence star) population than that from *Kepler*. The *TESS* sample is a closer match to the radial velocity sample of bright nearby stars and should provide another test for any tension in the occurrence rates derived by the two techniques.
2. The *TESS* sample spans A, F, and G main-sequence stars. By comparing the planet distribution around A and FG samples, we can determine if the paucity of close-in planets around “retired A stars” is due to post-main-sequence stellar evolution. More broadly, we can test

Table 7
Stellar Parameters

Parameter	HAT-P-69	HAT-P-70
Catalog Information		
TIC	379929661	399870368
Tycho-2	0215-01594-1	0688-01684-1
<i>Gaia</i> DR2	3080104185367102592	3291455819447952768
<i>Gaia</i> R.A. (2015.5)	08:42:01.353	04:58:12.560
<i>Gaia</i> Decl. (2015.5)	+03:42:38.038	+09:59:52.726
<i>Gaia</i> μ_α (mas yr ⁻¹)	-2.856 ± 0.074	-2.657 ± 0.096
<i>Gaia</i> μ_δ (mas yr ⁻¹)	0.984 ± 0.051	-4.996 ± 0.065
<i>Gaia</i> DR2 Parallax (mas)	2.902 ± 0.043	2.996 ± 0.061
Stellar atmospheric properties ^a		
T_{eff} (K)	7394 ⁺³⁶⁰ ₋₆₀₀	8450 ⁺⁵⁴⁰ ₋₆₉₀
[Fe/H]	-0.069 ^{+0.058} _{-0.075}	-0.059 ^{+0.075} _{-0.088}
$v \sin I_*$ (km s ⁻¹)	77.44 ^{+0.55} _{-0.57}	99.85 ^{+0.64} _{-0.61}
v_{macro} (km s ⁻¹)	5.76 ^{+0.24} _{-0.24}	5.870 ^{+0.58} _{-0.52}
Photometric properties		
<i>TESS</i> T (mag)	9.612 ± 0.018	9.298 ± 0.019
<i>Gaia</i> G (mag)	9.77216 ± 0.00035	9.45112 ± 0.00035
TYCHO B (mag)	10.052 ± 0.061	9.621 ± 0.045
TYCHO V (mag)	9.7740 ± 0.0050	9.4700 ± 0.0040
APASS g' (mag)	9.796 ± 0.030	9.842 ± 0.351
APASS r' (mag)	9.855 ± 0.041	9.506 ± 0.028
APASS i' (mag)	9.976 ± 0.020	9.962 ± 0.061
2MASS J (mag)	9.373 ± 0.024	9.068 ± 0.022
2MASS H (mag)	9.293 ± 0.022	9.023 ± 0.029
2MASS K_s (mag)	9.280 ± 0.023	8.963 ± 0.024
Stellar properties		
M_* (M_\odot)	1.648 ^{+0.058} _{-0.026}	1.890 ^{+0.010} _{-0.013}
R_* (R_\odot)	1.926 ^{+0.060} _{-0.031}	1.858 ^{+0.119} _{-0.091}
$\log g_*$ (cgs)	4.110 ^{+0.034} _{-0.064}	4.181 ^{+0.055} _{-0.063}
L_* (L_\odot)	10.0 ^{+1.8} _{-0.9}	16.7 ^{+5.3} _{-4.6}
Stellar oblateness $R_{\text{pole}}/R_{\text{eq}}$	0.9678 ^{+0.0012} _{-0.0022}	0.9574 ^{+0.0063} _{-0.0057}
Line of sight inclination I_*	58.2 ^{+1.6} _{-1.2}	58.8 ^{+7.5} _{-4.8}
$E(B - V)$ (mag) ^b	0.0167 ^{+0.011} _{-0.015}	<0.034(1 σ)
Age (Gyr)	1.27 ^{+0.28} _{-0.44}	0.60 ^{+0.38} _{-0.20}
Distance (pc)	343.9 ^{+4.8} _{-4.3}	329.0 ± 6.5

Notes.^a Derived from the global modeling described in Section 3, coconstrained by spectroscopic stellar parameters and the *Gaia* DR2 parallax.^b Uniform prior for reddening up to the local maximum set by Schlafly & Finkbeiner (2011).

whether the occurrence rates of hot Jupiters change with stellar mass.

4.1. Main-sequence Sample

We restricted our study to main-sequence stars. We did not wish to consider evolved stars because of the problems with selection biases, shallower transit depths, and lack of substantial follow-up observations. We do note, though, that more than half of the *TESS* stars brighter than 10th magnitude are evolved. Eventually, this will be a rich hunting ground (e.g., Huber et al. 2019; Rodriguez et al. 2019).

Figure 15 shows the color-magnitude diagram (CMD) of the 120,000 stars brighter than $T_{\text{mag}} = 10$ that were observed by *TESS*. The $B_p - R_p$ and G values are taken from a cross match

Table 8
Orbital and Planetary Parameters

Parameter	HAT-P-69 b	HAT-P-70 b
Light curve parameters		
P (days)	4.7869491 ^{+0.0000018} _{-0.0000021}	2.74432452 ^{+0.00000079} _{-0.00000068}
T_c (BJD-TDB) ^a	2458495.78861 ^{+0.00072} _{-0.00073}	2458439.57519 ^{+0.00045} _{-0.00037}
T_{14} (days) ^a	0.2136 ^{+0.0014} _{-0.0014}	0.1450 ^{+0.0028} _{-0.0020}
a/R_*	7.32 ^{+0.16} _{-0.18}	5.45 ^{+0.29} _{-0.49}
R_p/R_*	0.08703 ^{+0.00075} _{-0.00080}	0.09887 ^{+0.00133} _{-0.00095}
$b \equiv a \cos i/R_*$	0.366 ^{+0.060} _{-0.050}	-0.629 ^{+0.081} _{-0.054}
i (deg)	87.19 ^{+0.52} _{-0.72}	96.50 ^{+1.42} _{-0.91}
$ \lambda $ (deg)	21.2 ^{+4.6} _{-3.6}	113.1 ^{+5.1} _{-3.4}
Limb-darkening and gravity-darkening coefficients ^b		
a'_r (HAT) (linear term)	0.1194 (fixed)	0.1550 (fixed)
b'_r (HAT) (quadratic term)	0.3974 (fixed)	0.3306 (fixed)
a_{GC}	0.41 ^{+0.09} _{-0.10}	0.43 ^{+0.10} _{-0.10}
b_{GC}	0.25 ^{+0.09} _{-0.11}	0.25 ^{+0.09} _{-0.11}
a_{RC}	0.30 ^{+0.10} _{-0.09}	0.24 ^{+0.10} _{-0.09}
b_{RC}	0.21 ^{+0.10} _{-0.11}	0.19 ^{+0.10} _{-0.10}
a'_i	0.117 ^{+0.018} _{-0.018}	0.239 ^{+0.018} _{-0.021}
b'_i	0.392 ^{+0.020} _{-0.019}	0.338 ^{+0.021} _{-0.020}
a'_z	0.069 ^{+0.018} _{-0.018}	
b'_z	0.389 ^{+0.020} _{-0.020}	
a_{TESS}	0.238 ^{+0.021} _{-0.019}	0.149 ^{+0.018} _{-0.021}
b_{TESS}	0.286 ^{+0.015} _{-0.019}	0.313 ^{+0.019} _{-0.022}
β Gravity-darkening coefficient	0.239 ^{+0.026} _{-0.029}	0.242 ^{+0.026} _{-0.029}
RV parameters		
K (m s ⁻¹)	309 ⁺⁴⁹ ₋₄₉	<649(3 σ)
e	0 (fixed)	0 (fixed)
RV jitter (m s ⁻¹)	53 ⁺³⁴ ₋₃₇	320 ⁺¹⁸⁰ ₋₁₈₀
Systemic RV (m s ⁻¹) ^c	784 ± 24	25260 ± 110
Planetary parameters		
M_p (M_J)	3.58 ^{+0.58} _{-0.58}	<6.78 (3 σ)
R_p (R_J)	1.676 ^{+0.051} _{-0.033}	1.87 ^{+0.15} _{-0.10}
ρ_p (g cm ⁻³)	1.02 ^{+0.18} _{-0.16}	<1.54 (3 σ)
$\log g_p$ (cgs)	3.521 ^{+0.067} _{-0.071}	<3.73 (3 σ)
a (au)	0.06555 ^{+0.00070} _{-0.00035}	0.04739 ^{+0.00031} _{-0.00106}
T_{eq} (K) ^d	1930 ⁺⁸⁰ ₋₂₃₀	2562 ⁺⁴³ ₋₅₂

Notes.^a T_c : Reference epoch of midtransit that minimizes the correlation with the orbital period. T_{14} : total transit duration, time between first and last contact.^b Values for a quadratic law given separately for each of the filters with which photometric observations were obtained. These values were adopted from the tabulations by Claret & Bloemen (2011) according to the spectroscopic initial estimate of the stellar parameters. The limb-darkening coefficients are constrained by strong Gaussian priors of width 0.02 about their initial values. The gravity-darkening coefficient β is also constrained by a Gaussian prior of width 0.028 in the fit.^c The systemic RV for the system as measured relative to the telluric lines.^d T_{eq} calculated assuming zero albedo and full heat redistribution.

against the *Gaia* DR2 catalog (Gaia Collaboration et al. 2018). To define the main sequence, we make use of the colors and magnitudes from the MESA Isochrones and Stellar Tracks (MIST; Dotter 2016). We draw an upper and a lower boundary in the $B_p - R_p$ versus G diagram based on the zero-age main sequence (ZAMS) and the terminal-age main sequence (TAMS) points in the solar-metallicity MIST evolution tracks.

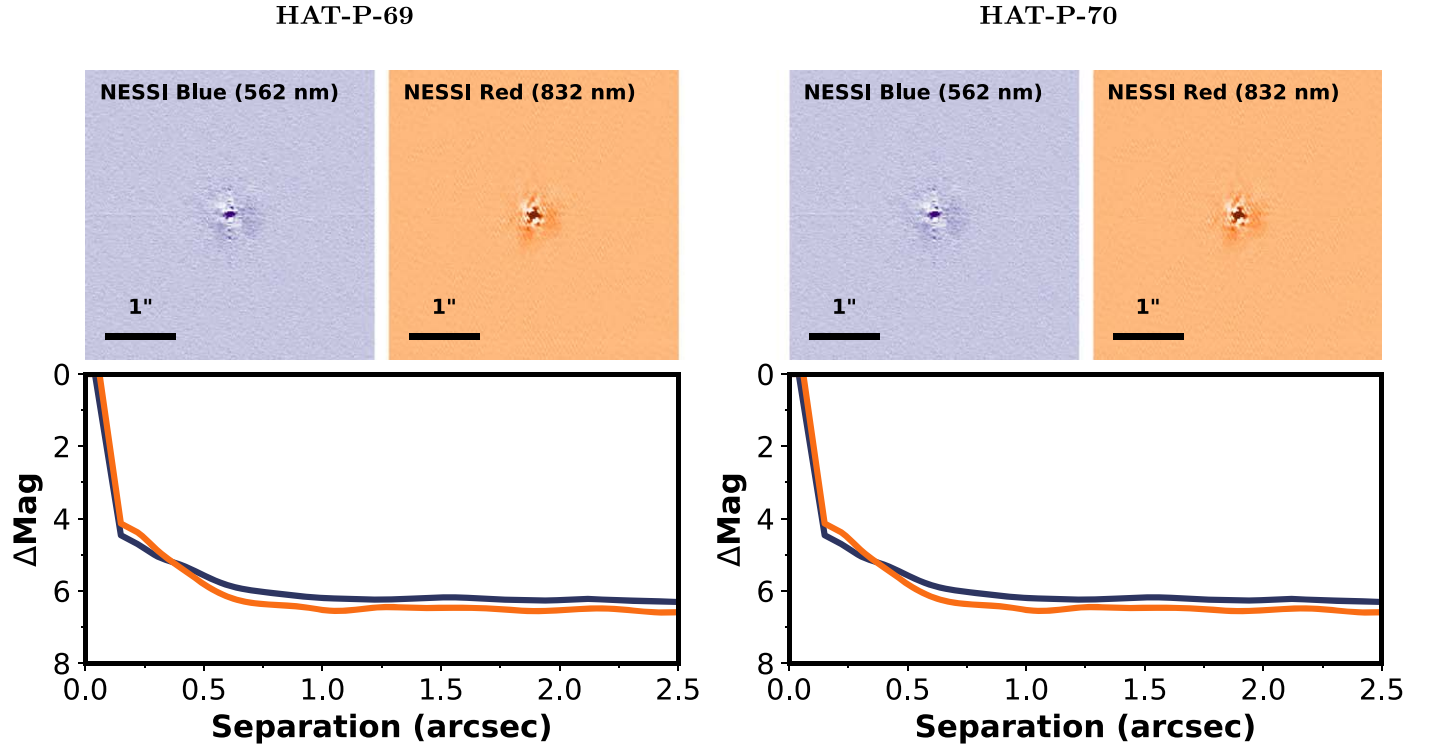


Figure 13. Images and constraints on spatially separated stellar companions via speckle imaging for HAT-P-69 and HAT-P-70 from NESSI. Companions with separations $\gtrsim 0''.04$ are ruled out. The blue and orange lines mark the 5σ limit on the detection of companions via the blue and red NESSI cameras.

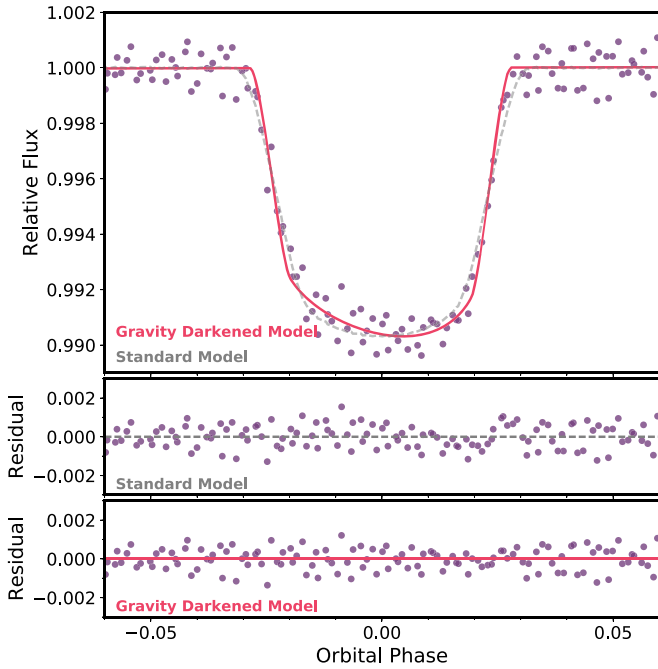


Figure 14. *TESS* transit light curve of HAT-P-70. Note that the transit is asymmetric, being shallower near ingress and deeper near egress. This is due to the planet traversing from the gravity-darkened equator to the brighter pole during the transit. The middle panel shows the light curve residual of a standard, symmetric transit model. There are systematic variations in the residuals due to the gravity-darkening effect. The bottom panel shows the residuals when the best-fit gravity-darkening model is subtracted.

As per Dotter (2016), the ZAMS is defined by the criterion that the core hydrogen luminosity of the star is 99.9% of the total core luminosity, while the TAMS is defined by the criterion

that the core hydrogen fraction has fallen below 10^{-12} . The ZAMS and TAMS boundaries are plotted in Figure 15. Between these boundaries, we are left with 47,126 main-sequence stars for this study.

The restriction to stars with $T_{\text{mag}} < 10$ allows us to make use of the TOI catalog available to the *TESS* follow-up community, which is essentially complete for hot Jupiters. The planet candidates around fainter stars in the FFIs are not fully vetted. We also restrict attention to the data from Sectors 1–7 because the candidates derived from later sectors have not yet received sufficient follow-up observations at the time of writing.

To check our CMD-derived stellar parameters and to estimate the metallicity of the population, we cross-match our field stellar population against the *TESS*-HERMES DR1 spectroscopic parameters for stars in the *TESS* southern continuous viewing zone (Sharma et al. 2018). Because the initial data release is restricted to stars within $10 < V < 13.1$, we expect a very limited number of matches. We find 491 stars to have stellar parameters from *TESS*-HERMES within our sample, of which 301 have rotational broadening velocities $v \sin I_* < 20 \text{ km s}^{-1}$. Figure 16 shows a comparison between our stellar effective temperature, surface gravity, and stellar mass against the spectroscopically measured values from *TESS*-HERMES.

The median absolute deviations (MADs) between CMD and spectroscopic parameters are 60 K in T_{eff} , 0.09 dex in $\log g$, and $0.09 M_{\odot}$ in mass. However, we notice a systematic offset in our effective temperature and mass estimates for cool stars (dotted line in Figure 16). We correct for this bias by fitting for a polynomial correction to our parameters as follows for temperature:

$$T_{\text{eff}} = 0.49 T_{\text{eff,CMD}} + 1958 \quad (1)$$

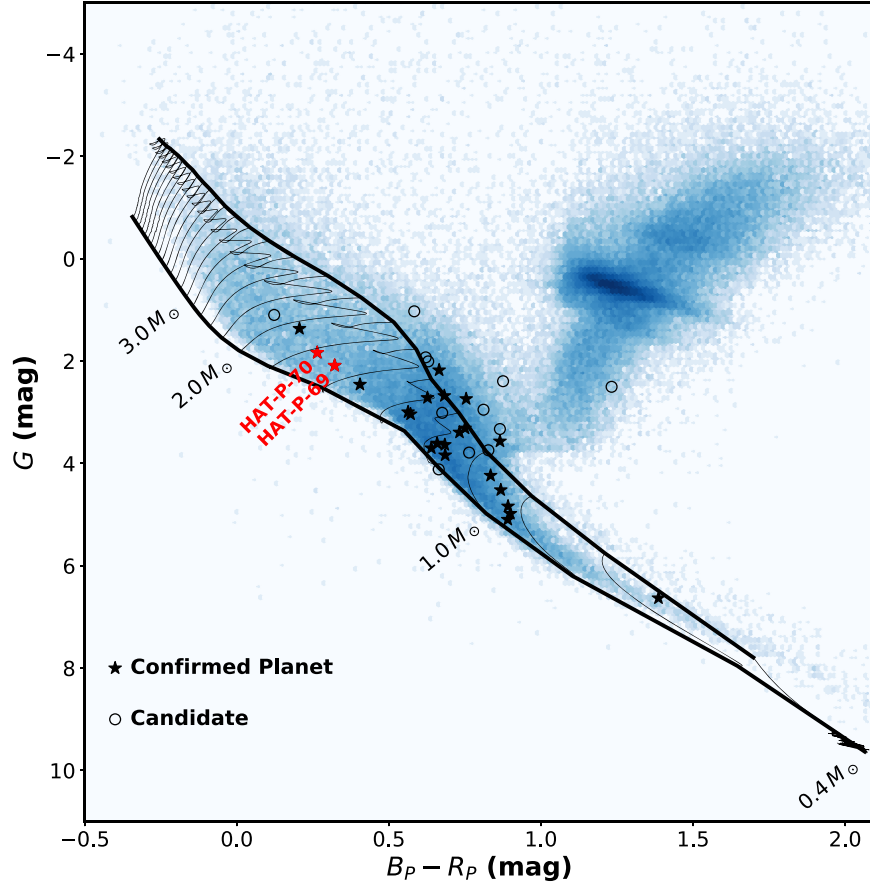


Figure 15. *Gaia* CMD for stars brighter than $T_{\text{mag}} = 10$ observed within the first seven sectors of the *TESS* mission. The ZAMS (lower) and TAMS (upper) boundaries are plotted to mark the main sequence. Evolution tracks from the MIST isochrones (Dotter 2016) spaced at $0.2 M_{\odot}$ intervals are plotted across the main sequence. Close-in giant planets discovered or recovered by *TESS* are plotted, marked in solid stars for confirmed planets and open circles for planet candidates. Planet candidates off the main sequence, or around cool stars, but in the *TESS* Objects of Interest are plotted on this diagram for completeness, but not included in the analysis.

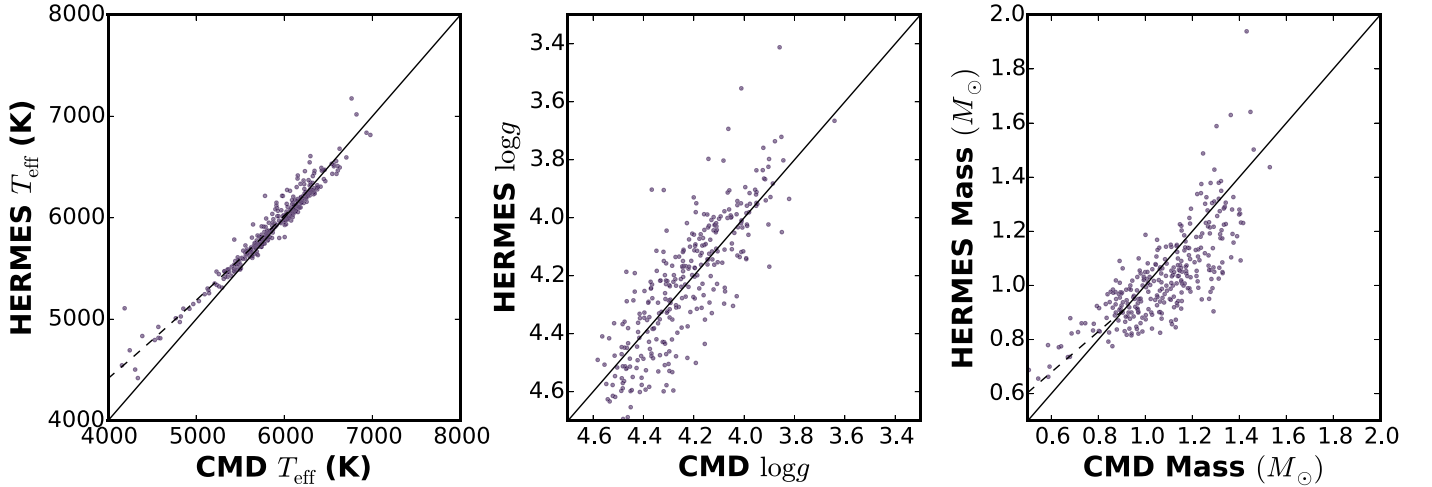


Figure 16. Comparison between *Gaia* CMD-derived stellar parameters and those from *TESS*-HERMES. We find 301 slowly rotating stars ($v \sin i_{*} < 20 \text{ km s}^{-1}$) within our sample that have stellar parameters from *TESS*-HERMES data release 1. We find a general consistency between the parameters, but apply a correction to our CMD-derived T_{eff} and M_{*} of cool stars (marked by the dashed lines).

for stars with $4000 < T_{\text{eff,CMD}} < 6120 \text{ K}$. We also apply a correction in mass:

$$M_{*} = 0.75 M_{*,\text{CMD}} + 0.23 \quad (2)$$

for $0.60 < M_{*,\text{CMD}} < 0.92 M_{\odot}$. Postcorrection, we find that MADs between CMD and spectroscopic parameters are 40 K in

T_{eff} and $0.08 M_{\odot}$ in mass. Figure 17 shows the properties of the stellar population included in our sample. The sample is grouped into mass bins roughly corresponding to the A ($1.4\text{--}2.3 M_{\odot}$), F ($1.05\text{--}1.4 M_{\odot}$), and G ($0.8\text{--}1.05 M_{\odot}$) spectral types. We elaborate on the occurrence rates of planets within each mass bin in Sections 4.3 and 4.4.

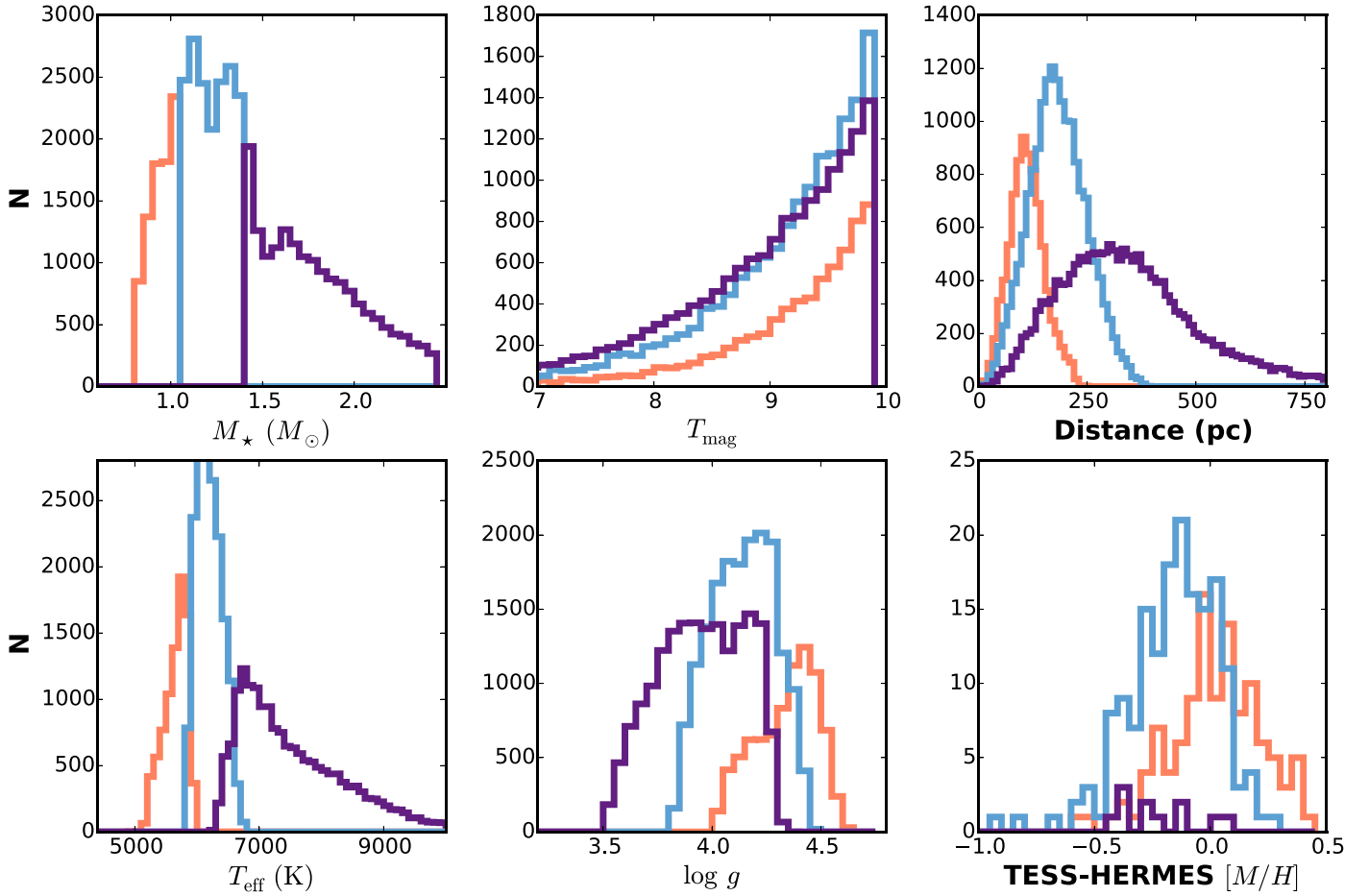


Figure 17. Properties of the stellar population included in our sample, including mass (M_*), brightness (T_{mag}), distance, effective temperature (T_{eff}), surface gravity ($\log g$), and metallicity ($[\text{Fe}/\text{H}]$). The population is subdivided into mass bins roughly corresponding to the A ($1.4\text{--}2.3 M_\odot$; purple), F ($1.05\text{--}1.6 M_\odot$; cyan), and G ($0.8\text{--}1.05 M_\odot$; orange) spectral types. Metallicity measurements come from the 301 stars within our sample that have *TESS*-HERMES measurements.

In particular, the metallicity distributions of the 301 stars with *TESS*-HERMES measurements are plotted. We note that the population has near-solar metallicity of $[\text{Fe}/\text{H}] = -0.06 \pm 0.21$. When subdivided into the mass bins, we find the G star bin to have $[\text{Fe}/\text{H}] = -0.03 \pm 0.20$, F stars to have $[\text{Fe}/\text{H}] = -0.13 \pm 0.19$, and A stars to have $[\text{Fe}/\text{H}] = -0.26 \pm 0.15$. We note that when subdivided into their mass bins, the number of stars per bin becomes very small and may not be representative of the population. We look forward to further fields of the *TESS*-HERMES being completed, as well as similar surveys of brighter stars, to allow a better examination of the dependence between metallicity and the *TESS* planet properties.

4.2. Candidate Identification

Our planet sample makes use of the candidates (TOIs) released by the *TESS* Science office from the first seven sectors of *TESS* data around stars brighter than $T_{\text{mag}} = 10$. The TOIs are selected from a list of threshold crossing events (TCEs) by human vetters. A TCE requires the signal-to-noise ratio of the planet to be above 7.3 and that at least two transits are detected in the light curve. The human vetters reject some false positives based on standard diagnostics. For example, these may include large secondary eclipse/phase variation detections that indicate the eclipsing object is of stellar nature, an obvious centroid offset detection that indicates the eclipsing events happened on

a background object, or significant depth variation with the choice of photometric aperture. We also cross-reference the TCEs with known false positive/eclipsing binary catalogs (Triaud et al. 2017; Collins et al. 2018). Although the initial TOIs were generated from two different sources (the 2 minute and the 30 minute data), for uniformity we ensured that all of the TOIs we used in this work are detected as TCEs through the quick-look pipeline, and that all of the TCEs detected by the quick-look pipeline around stars brighter than $T_{\text{mag}} = 10$ mag went through the TOI process.

We define our hot Jupiter candidates as TOIs with an orbital period between 0.9 and 10 days, a radius between 0.8 and $2.5 R_{\text{Jup}}$, and a transit impact parameter smaller than 0.9. The period lower bound of 0.9 days was adopted to incorporate WASP-18b (Hellier et al. 2009), the shortest-period known hot Jupiter within *TESS* sectors 1–7 (Shporer et al. 2019), into our sample. A similar minimum period cut-off was also employed by Howard et al. (2012; 0.7 days) and Fressin et al. (2013; 0.8 days). We also note that no hot Jupiter candidates were found with periods < 0.9 days within our sample. To ensure a clean sample, we also require candidates to have a signal-to-noise ratio (S/N) larger than 10, although, in practice, none of the giant planet candidates have an S/N between 10 and the traditional value of 7.3. We use the stellar radii interpolated from the *Gaia* CMD (Section 4.1) to recompute the radius of the planet during the selection.

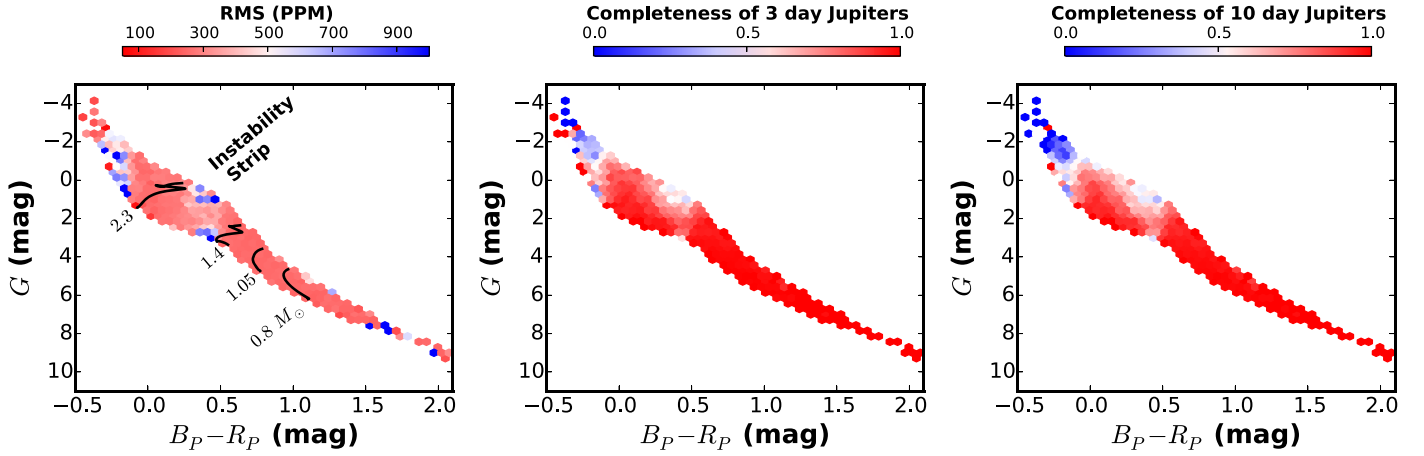


Figure 18. Left: median light curve scatter across the main sequence. Evolution tracks for 0.8, 1.05, 1.4, and 2.3 M_{\odot} solar-metallicity stars are plotted. The region near 1.6 M_{\odot} exhibits higher levels of scatter than average due to stars in the instability strip. Survey completeness for a 3 day period (center panel) and 10 day period (right) Jupiter-sized planet are plotted. We find that we are 80% complete for 10 day period hot Jupiters across the lower main sequence ($< 1.4 M_{\odot}$), and 70% complete for such planets around intermediate-mass stars ($1.4 < M_{\star} < 2.3 M_{\odot}$).

4.3. Completeness and Signal-to-noise Ratio Estimates

Since the expected noise floor for a typical *TESS* star at $T_{\text{mag}} = 10$ per 1 hr is 200 ppm (Huang et al. 2018), any giant planet transiting a main-sequence star in our sample should be detected with a high S/N. However, some stars may exhibit large amplitude and short timescale stellar variability, such as stars on the instability strip of the CMD. Strong stellar variability can reduce the sensitivity to transit signals. To estimate our completeness rate more accurately, we measured the per-point MAD σ_{mad} of detrended/deblended light curves for all of the 47,126 stars used in this paper, derived from the FFIs using the quick-look pipeline. A factor of 1.48 is applied to σ_{mad} such that it approximates the standard deviation scatter of the light curves. The S/N of the candidates is then estimated with

$$\text{S/N} = \frac{\delta}{1.48 \times \sigma_{\text{mad}}} \left(\frac{T_{\text{dur}} N_{\text{tr}}}{0.5} \right)^{0.5}, \quad (3)$$

where δ is the approximate transit depth, T_{dur} is the full transit duration in hours, and N_{tr} is the number of transits that appeared in the data from *TESS* Sectors 1–7.⁵⁰ We assume any planet with a calculated S/N exceeding 10 was selected as a candidate, and otherwise was not selected. We also assume that the hot Jupiters exhibit a uniform distribution in transit impact parameter between 0 and 0.9. Figure 18 shows the survey completeness for a Jupiter-sized planet with an impact parameter of 0.45, for both 3 and 10 day orbits. The transit duration is calculated under the assumption of a circular orbit. While this assumption may not be valid for planets with periods approaching 10 days, it has been shown that modestly eccentric orbits have a negligible effect on survey completeness (Burke 2008).

⁵⁰ We have taken into account the actual duty cycles in each *TESS* sector by only using the light curve available to the Box Least Search in the quick-look pipeline. This is the light curve length after accounting for bad point masking due to scattered light, pointing jitter, and data downlink gap. The number of days used in each of these seven sectors are 21.5, 21.4, 16.5, 15.3, 21.5, 17.3, and 21.5.

4.4. Results

A total of 47,126 stars and 31 TOIs are included in the occurrence rate calculation. The TOIs are composed of 18 confirmed planets, 3 planet candidates, and 10 false positives. The lists of planets, candidates, and false positives are given in the Appendix. To summarize the previous sections, the stellar and planet population is defined within the criteria below:

1. Brighter than $T_{\text{mag}} = 10$.
2. Lying within the solar-metallicity ZAMS and TAMS boundaries on the *Gaia* $B_P - R_P$ versus G CMD, and thereby classified as main sequence.
3. Planets are detected with BLS S/N > 10 and passed the vetting process.
4. Planets with periods $0.9 \leq P \leq 10$ days.
5. Planets with radii $0.8 \leq R_p \leq 2.5 R_{\text{Jup}}$.
6. Transits with impact parameter $b < 0.9$ to avoid grazing transits.

Within this stellar sample, the population is binned by stellar mass into A (1.4–2.3 M_{\odot}), F (1.05–1.4 M_{\odot}), and G (0.8–1.05 M_{\odot}) spectral types. We estimate the occurrence rate f within each stellar mass bin as the conjugate distribution of the binomial distribution (i.e., the beta distribution):

$$\mathcal{P}(f) = \text{Beta}(n_{\text{obs}}, n_{\text{trial}} - n_{\text{obs}}), \quad (4)$$

in which n_{obs} is the number of transiting planets observed in the mass bin, and n_{trial} is the effective number of times we try to conduct the detection of those transiting planets after accounting for transit probability and completeness. Specifically,

$$n_{\text{obs}} = \sum_{i=1, n_p} (1 - \text{FP}_i) w_i, \quad (5)$$

where w_i is a weight indicating the probability that a planet/candidate falls within a particular mass bin. The probability distribution for the mass of each planet/candidate host star is modeled as a Gaussian distribution centered on the estimated mass, with a dispersion equal to 10% of the value of the estimated mass. The false-positive rate FP is estimated in each stellar mass bin using current follow-up results and is only

applied to the active candidates. For the confirmed planets, the false-positive rate is set equal to zero. The false-positive rate is applied only to the active planet candidates, while $FP = 0$ for confirmed planets. The false-positive rate is calculated per stellar mass bin as

$$FP = \frac{N_{\text{False positives}}}{N_{\text{Confirmed Planets}} + N_{\text{False Positives}}}. \quad (6)$$

Based on the photometric and spectroscopic observations that have been performed so far by the *TESS* follow-up program, we find a false-positive rate of 15% for G stars, 41% for F stars, and 47% for A stars. Globally, the false-positive rate for hot Jupiters from *TESS* within our sample is 35%. Similar false-positive rates for short-period giant planets (29.3%) were reported by Fressin et al. (2013) for the initial *Kepler* candidates. The uncertainty assumes Poisson errors based on the number of planet candidates and false positives surveyed so far.

We define n_{trial} as

$$n_{\text{trial}} = \sum_{i=1, n_*} \int \mathcal{P}_{\text{tran}} \mathcal{P}_{\text{det}} dP dR, \quad (7)$$

in which n_* is the total number of observed stars falling in a particular mass bin, and $\mathcal{P}_{\text{tran}}$ and \mathcal{P}_{det} are the probability of a planet with period P and radius R transiting and being detected around star i , respectively. The transit probability for a planet with period P around a star with radius r_i and mass m_i is

$$\mathcal{P}_{\text{tran},i}(P) = 0.9 r_i \left(\frac{2\pi}{P} \right)^{2/3} (G m_i)^{-1/3}. \quad (8)$$

The coefficient of 0.9 is present because we only consider planets and candidates with impact parameters smaller than 0.9. The probability of detection for each star is estimated following Section 4.3, assuming any planet with $S/N \leq 10$ has been detected. The final integration is computed using a Monte Carlo method assuming that the intrinsic period distribution of a planet is uniform within the range from 0.9 to 10 days and the radius distribution of a planet is uniform within the range from 0.8 to 1.5 R_{Jup} .

Figure 19 summarizes the planet sample, search completeness, and field star population within each spectral-class mass bin.

This planet and host star sample yields a total hot Jupiter occurrence rate from *TESS* of $0.41 \pm 0.10\%$. Within each mass bin, we find an occurrence rate of $0.71 \pm 0.31\%$ for main-sequence G stars, $0.43 \pm 0.15\%$ for F stars, and $0.26 \pm 0.11\%$ for A stars. These occurrence rates are presented in Figure 20.

In this analysis, we defined the main sequence as being bound within the solar-metallicity ZAMS and TAMS lines. The actual population should exhibit a dispersion in metallicity, with the effect of stars being brighter at higher metallicity for the same evolutionary state, and vice versa for lower metallicity stars. To test the effect of a more blurred main-sequence boundary, we reperformed the analysis while assuming a $[\text{Fe}/\text{H}] = -0.27$ ZAMS boundary and a $[\text{Fe}/\text{H}] = +0.15$ TAMS boundary, encompassing the 1σ dispersion in metallicity seen in our cross-matched *TESS*-HERMES stars. The resulting main-sequence sample increased to 52,788 stars and included two additional confirmed planets around F stars, two new

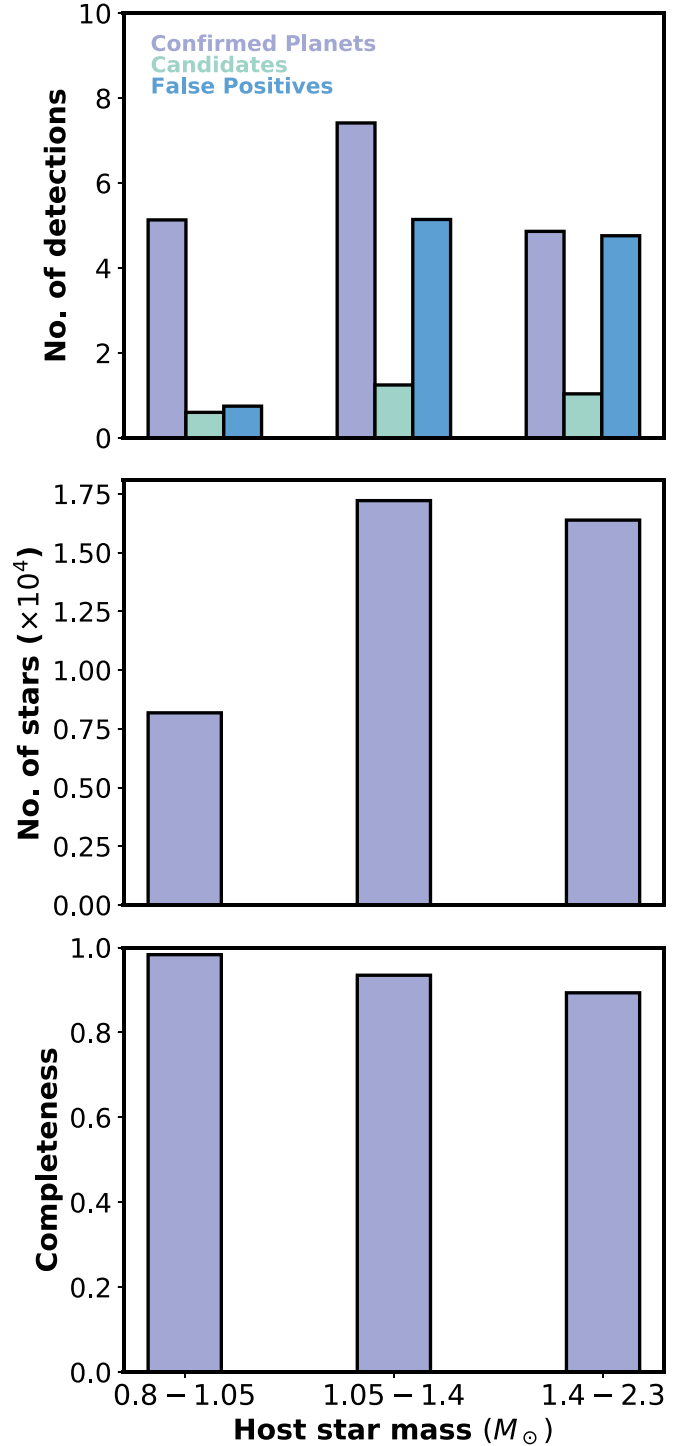


Figure 19. Sample size and completeness for each range of stellar mass. Top: number of confirmed planets, candidates, and false positives for each range of stellar mass. The noninteger number of detections within each bin is due to the mass uncertainty of each host star being taken into account. Center: stellar sample size (in 10^4 stars). Bottom: planet detection completeness for a 10 day Jupiter-sized planet.

candidates about G stars, one new candidate around an F star, and one new candidate around an A star. The net result is no significant change in the occurrence rates within each mass bin, nor any significant change for the whole sample.

Some caution may be necessary when directly comparing our occurrence rate against that derived from *Kepler* data. Our

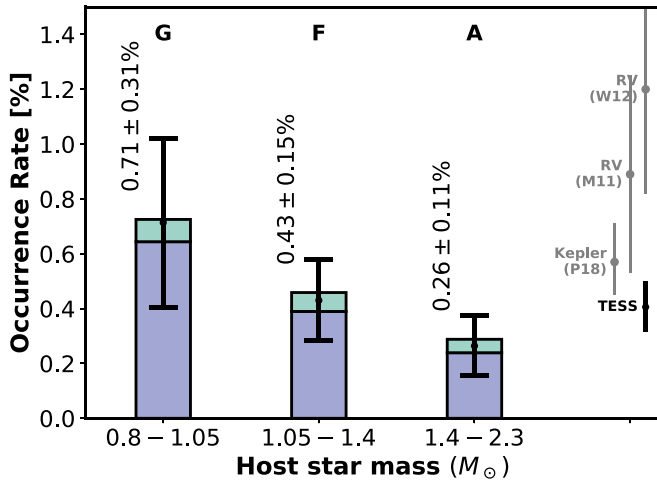


Figure 20. Occurrence rates of hot Jupiters across the main sequence as measured by *TESS*. The dark blue bars mark the occurrence rates from confirmed planets only, and cyan bars mark the occurrence rates if we assume that all unconfirmed planet candidates are true planets. The center of each error bar marks the expected occurrence rate taking into account the false-positive rate from follow-up observations to date. The expected occurrence rate of each mass bin is labeled. We find a total occurrence rate of $0.41 \pm 0.10\%$ for the entire sample. For comparison, the occurrence rates of hot Jupiters from *Kepler* ($0.57^{+0.14}_{-0.12}\%$ from P18, Petigura et al. 2018) and radial velocity surveys ($0.89 \pm 0.36\%$ from M11, Mayor et al. 2011; $1.20 \pm 0.38\%$ from W12, Wright et al. 2012) are marked.

stellar sample is restricted to the main-sequence stars, while the *Kepler* sample may contain more evolved stars (Wang et al. 2015). Our definition of the main sequence is also different from more traditional definitions, which are based on surface gravity. We do not impose a surface gravity criterion because stars on the main sequence have different surface gravities at different masses: an intermediate-age main-sequence K star has $\log g \approx 4.5$, while A stars have $\log g \approx 3.8$ at the same evolutionary stage. Some previous works required $\log g < 3.9$ or 4.0 to define the main sequence, which may remove 10%–30% of the main-sequence population in the range $6000 < T_{\text{eff}} < 6500$ K (e.g., Howard et al. 2012; Petigura et al. 2018). We find that if we apply a limit of $\log g < 4.0$ to our sample, we increase the occurrence rates of hot Jupiters around F and A stars by nearly a factor of 2.

Although *TESS* is largely complete for hot Jupiters around F and G stars, the sensitivity is poorer for more evolved early A stars, for which the stellar radius can be as large as $4 R_{\odot}$. To check the dependence of our results on the completeness calculations, we tried drawing a boundary around smaller-radius A stars (defined by the boundary between $-0.1 < B_p - R_p < 0.5$ and $G > G_{\text{ZAMS}} - 1.0$). For stars within this boundary, the completeness is 80% for hot Jupiters with a period of 10 days. All of the confirmed cases of hot Jupiters around A stars that were used in our preceding calculations also reside within this more restricted sample. We find no significant difference ($< 1\sigma$) in the occurrence rates presented above and those obtained within this “near-complete” box.

Unrecognized binaries in the main-sequence population can cause systematic errors in occurrence rate estimates. Bouma et al. (2018) found that systematic biases due to binarity may be important for small planets, but for *Kepler* hot Jupiters the bias is only at the level of $\sim 5\%$, smaller than our current uncertainties. Our occurrence rates were also obtained for a main sequence defined between the ZAMS and TAMS

boundaries, which has the effect of removing some binaries because they appear overluminous. In testing for the effect of metallicity on our occurrence rates, we shifted the ZAMS and TAMS boundaries, but found minimal effect on the resulting occurrence rates.

A number of caveats still exist. The number of hot Jupiters around bright stars to be identified or recovered by *TESS* over the course of its mission will be at least four times that presented in this paper. We expect these occurrence rates and false-positive rates to be revised over the course of the mission. In particular, the majority of new hot Jupiters from *TESS* should be around intermediate-mass stars; the ground-based transit surveys are the least complete, and the hot Jupiter follow-up effort is most expensive within this regime. The uncertainties in our occurrence rates are currently dominated by Poisson statistics.

5. Conclusions

5.1. Agreement of *TESS* and *Kepler* Hot Jupiter Occurrence Rates

We find good agreement between the occurrence rates of hot Jupiters derived from the *TESS* and *Kepler* surveys. The occurrence rate from *TESS* is $0.41 \pm 0.10\%$. From *Kepler*, various studies have found occurrence rates of $0.4 \pm 0.1\%$ (Howard et al. 2012), $0.43 \pm 0.05\%$ (Fressin et al. 2013), $0.57^{+0.14}_{-0.12}\%$ (Petigura et al. 2018), and $0.43^{+0.07}_{-0.06}\%$ (Masuda & Winn 2017).

The number of stars and planets within the *TESS* sample is already comparable to that from the *Kepler* sample and will soon grow. We make use of 47,126 stars and 18 planets and 3 active candidates. Previously determined occurrence rates of hot Jupiters were computed from 24 planet candidates around 58,000 stars by Howard et al. (2012), and out of 14 planets around 37,000 stars by Petigura et al. (2018). The light curve precision that *TESS* provides for these bright stars is also comparable to that for the relatively fainter stars from the *Kepler* sample.

Our initial estimates of the sample metallicity, derived from a cross match of the bright *TESS* stars against the *TESS*-HERMES (Sharma et al. 2018) catalog, suggest that our sample ($[\text{Fe}/\text{H}] = -0.06 \pm 0.21$) is similar to that of *Kepler* (-0.045 ± 0.009 ; Guo et al. 2017). Future southern spectroscopic surveys of bright stars will continue to improve our understanding of the properties of field stars surveyed by *TESS*.

The average solar-type star from this *TESS* sample is located at 150 pc, while that observed by *Kepler* would be located at 400 pc (Mathur et al. 2017). Past surveys of more distant fields around the galactic bulge and disk (Gould et al. 2006; Bayliss & Sackett 2011) also found occurrence rates of hot Jupiters to be compatible with the rates derived from *Kepler* and *TESS* data, suggesting that there is not too much variety in the occurrence of hot Jupiters across the Galaxy.

We also remark on the near-completeness of the ground-based surveys. Of the 18 confirmed hot Jupiters within our sample, 13 were already discovered by the WASP (Pollacco et al. 2006), HATNet (Bakos et al. 2004), and KELT (Pepper et al. 2012) consortiums. Future studies of hot Jupiter properties from *TESS* will continue to capitalize on the follow-up efforts already made by these surveys.

5.2. No Evident Dependence on Stellar Mass

The occurrence rates of hot Jupiters within our A, F, and G mass bins agree with each other to within 1σ . Hot Jupiters are just as abundant around main-sequence A stars as they are around F and G stars. Radial velocity surveys have reported a paucity of giant planets in close-in orbits about “retired A stars.” Together this seems to support the conclusion that enhanced tidal dissipation within evolved stars accelerates the process of tidal orbital decay of hot Jupiters (Schlaufman & Winn 2013). Post-main-sequence tidal evolution may be strongly dependent on the mass of the planets (e.g., Villaver & Livio 2009; Villaver et al. 2014), and more stringent constraints on the distribution of these main-sequence close-in giant planets may help yield additional clues into the tidal model for hot Jupiters. We note, though, that sample sizes of the Doppler surveys ranged from 166 stars (Jones et al. 2014) to 373 stars (Reffert et al. 2015), small enough that one should only expect ~ 1 hot Jupiter to be found even if stellar evolution has no effect on the hot Jupiter occurrence rate. The Doppler surveys also noted an enhanced planet fraction for longer-period gas giants about more massive stars. Ghezzi et al. (2018) notes a $2\times$ increase in planet fraction about $2M_{\odot}$ stars compared to solar-mass stars, while Johnson et al. (2010) noted a nearly $3\times$ increase in the planet fraction within the $1\text{--}2M_{\odot}$ host mass range. Curiously, the hot Jupiter occurrence rate does not reflect this trend. Hot Jupiters are no more abundant about A stars than they are about F and G stars. Since the planets around early-type stars exhibit a wide distribution of obliquity angles (Albrecht et al. 2012), this may point to a lack of stellar mass preference for the dynamical migration of hot Jupiters.

We thank the referee for their careful reading of the manuscript; the comments significantly improved the quality of the paper. Work by G.Z. is provided by NASA through Hubble Fellowship grant HST-HF2-51402.001-A awarded by the Space Telescope Science Institute, which is operated by the Association of Universities for Research in Astronomy, Inc., for NASA under contract NAS 5-26555. HATNet operations have been funded by NASA grants NNG04GN74G and NNX13AJ15G. Follow-up of HATNet targets has been partially supported through NSF grant AST-1108686. G.Á.B., Z.C., and K.P. acknowledge partial support from NASA grant NNX09AB29G. J.H. acknowledges support from NASA grant NNX14AE87G. K.P. acknowledges support from NASA grants 80NSSC18K1009 and NNX17AB94G. We acknowledge partial support also from the *Kepler* Mission under NASA Cooperative Agreement NNX13AB58A (D.W.L., PI). Data presented in this paper are based on observations obtained at the HAT station at the Submillimeter Array of SAO, and the HAT station at the Fred Lawrence Whipple Observatory of SAO. This research has made use of the NASA Exoplanet Archive, which is operated by the California Institute of Technology, under contract with the National Aeronautics and Space Administration under the Exoplanet Exploration Program. Observations on the LCO 1 m network were made through NOAO program 2017B-0039, and time on the WIYN 3.5 m was awarded through NOAO programs 2016B-0078 and 2017A-0125. Observations on the SMARTS 1.5 m CHIRON

facility were made through the NOAO program 2019A-0004. M.G. and E.J. are FNRS Senior Research Associates. The research leading to these results has received funding from the grant for Concerted Research Actions, financed by the Wallonia-Brussels Federation. Funding for the *TESS* mission is provided by NASA’s Science Mission directorate. We acknowledge the use of public *TESS* Alert data from pipelines at the *TESS* Science Office and at the *TESS* Science Processing Operations Center. This research has made use of the Exoplanet Follow-up Observation Program website, which is operated by the California Institute of Technology, under contract with the National Aeronautics and Space Administration under the Exoplanet Exploration Program. This paper includes data collected by the *TESS* mission, which are publicly available from the Mikulski Archive for Space Telescopes (MAST). G.K. is grateful for the support from the National Research, Development and Innovation Office (grant K 129249). G.K. is grateful for the support from the National Research, Development and Innovation Office (grant K 129249). The observations by the CHIRON spectrograph have been supported by the grant of the Hungarian Scientific Research Fund (OTKA, K-81373) to G.K. WASP-South is hosted by the South African Astronomical Observatory, and we are grateful for their ongoing support and assistance. Funding for WASP comes from consortium universities and from the UK’s Science and Technology Facilities Council. Work by J.N.W. was supported by the Heising-Simons Foundation. This work is partly supported by JSPS KAKENHI grant Nos. JP18H01265 and JP18H05439, and JST PRESTO grant No. JPMJPR1775. Observations in the paper made use of the NN-EXPLORE Exoplanet and Stellar Speckle Imager (NESSI). NESSI was funded by the NASA Exoplanet Exploration Program and the NASA Ames Research Center. NESSI was built at the Ames Research Center by Steve B. Howell, Nic Scott, Elliott P. Horch, and Emmett Quigley. I.W. is supported by a Heising-Simons *51 Pegasi b* postdoctoral fellowship. A. K. acknowledges support from the National Research Foundation (NRF) of South Africa. Some of the observations reported in this paper were obtained with the Southern African Large Telescope (SALT).

Facilities: HATNet, FLWO 1.5 m, CTIO:1.5m, *TESS*, SALT.

Software: lightkurve (Barentsen et al. 2019), emcee (Foreman-Mackey et al. 2013), simultrans (Herman et al. 2018), Astropy (Astropy Collaboration et al. 2013, 2018), fitsh (Pál 2012).

Appendix Planets and Planet Candidate

We tabulate here all TOIs that made up the numerator of our occurrence rate calculation. Table 9 presents the confirmed planets, Table 10 shows the planet candidates and their follow-up stats, Table 11 shows the false positives, and Table 12 shows the confirmed giant planets orbiting stars $T_{\text{mag}} < 10$ that were not included in the sample due to the evolved states of their host stars. The planet and candidate lists are up-to-date as of 2019 June and can be accessed via tev.mit.edu.

Table 9
Confirmed Planets with $T_{\text{mag}} < 10$

TIC	TOI	Name	Status ^a	Period (days)	Depth (ppm)	<i>Gaia</i> G (mag)	<i>Gaia</i> B_P (mag)	<i>Gaia</i> R_P (mag)	Distance (pc)	T_{eff}^b (K)	M_* (M_{\odot})	R_* (R_{\odot})	References
1129033	398.01	WASP-77A	P	1.4	16380	10.1	10.48	9.59	105	5433	0.91	0.98	Maxted et al. (2013)
25375553	143.01	WASP-111	P	2.3	6939	10.11	10.36	9.73	300	6305	1.3	2.03	Anderson et al. (2014)
47911178	471.01	WASP-101	P	3.6	12321	10.14	10.41	9.75	202	6209	1.16	1.39	Hellier et al. (2014)
65412605	626.01	KELT-25	P	4.4	5812	9.6	9.68	9.47	442	7983	1.92	2.39	R. Rodriguez et al. (2019, in preparation)
92352620	107.01	WASP-94A	P	4.0	12999	10.03	10.33	9.6	212	5949	1.16	1.67	Neveu-VanMalle et al. (2014)
100100827	185.01	WASP-18	P	0.9	10692	9.17	9.43	8.79	123	6291	1.16	1.3	Hellier et al. (2009)
144065872	105.01	WASP-95	P	2.2	11836	9.94	10.29	9.46	138	5627	0.99	1.28	Hellier et al. (2014)
149603524	102.01	WASP-62	P	4.4	14034	10.07	10.36	9.67	176	6123	1.13	1.29	Hellier et al. (2012)
166836920	267.01	WASP-99	P	5.8	5386	9.33	9.64	8.89	159	5894	1.16	1.77	Hellier et al. (2014)
170634116	413.01	WASP-79	P	3.7	12455	9.97	10.2	9.63	248	6571	1.38	1.65	Smalley et al. (2012)
183532609	191.01	WASP-8	P	8.2	15535	9.61	10.0	9.11	90	5455	0.89	1.04	Queloz et al. (2010)
201248411	129.01	...	P	1.0	7028	10.59	11.23	9.85	61	4216	0.5	0.81	L. Nielsen et al. (2019, in preparation)
230982885	195.01	WASP-97	P	2.1	13510	10.42	10.79	9.92	151	5526	0.9	1.17	Hellier et al. (2014)
267263253	135.01	...	P	4.1	10068	9.52	9.75	9.18	197	6538	1.37	1.63	Jones et al. (2019)
379929661	625.01	HAT-P-69	P	4.8	7627	9.77	9.9	9.58	344	7532	1.68	1.92	This work
399870368	624.01	HAT-P-70	P	2.7	8443	9.45	9.55	9.29	333	7818	1.77	2.03	This work
425206121	508.01	KELT-19A	P	4.6	10364	9.86	10.0	9.6	302	7188	1.52	1.77	Sivervd et al. (2018)
455135327	490.01	HAT-P-30	P	2.8	10758	10.3	10.58	9.89	215	6116	1.12	1.42	Johnson et al. (2011)

Notes.

^a P: Confirmed planet.

^b Parameters T_{eff} , M_* , and R_* from isochrone interpolation of the *Gaia* color–magnitude values. These can deviate from literature values but are consistent with the remainder of the analysis of the field star population.

Table 10
Planet Candidates

TIC	TOI	Status ^a	Period (days)	Depth (ppm)	<i>Gaia</i> <i>G</i> (mag)	<i>Gaia</i> <i>B_P</i> (mag)	<i>Gaia</i> <i>R_P</i> (mag)	Distance (pc)	<i>T</i> _{eff} (K)	<i>M</i> _* (<i>M</i> _⊙)	<i>R</i> _* (<i>R</i> _⊙)	Follow-up Status
129637892	155.01	PC	5.4	8232	9.38	9.66	8.98	188	6144	1.26	1.87	Passed spectroscopic vetting
281408474	628.01	PC	3.4	6353	10.06	10.38	9.61	179	5850	1.05	1.45	Undergoing spectroscopic vetting
293853437	629.01	PC	8.7	2075	8.73	8.79	8.66	336	8400	2.06	2.49	Undergoing spectroscopic vetting


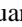


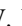
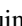
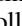
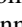




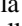



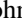

Note.^a PC: Active planet candidate.**Table 11**
Candidates Determined to Be False Positives



TIC	TOI	Status ^a	Period (days)	Depth (ppm)	<i>Gaia</i> <i>G</i> (mag)	<i>Gaia</i> <i>B_P</i> (mag)	<i>Gaia</i> <i>R_P</i> (mag)	Distance (pc)	<i>T</i> _{eff} (K)	<i>M</i> _* (<i>M</i> _⊙)	<i>R</i> _* (<i>R</i> _⊙)
7624182	412.01	NEB	1.1	859	8.83	8.87	8.77	466	8099	2.2	3.28
14091633	447.01	SB1	5.5	20670	9.2	9.46	8.83	126	6316	1.17	1.3
49899799	416.01	SB1	7.0	7442	8.65	8.94	8.24	132	6065	1.23	1.89
55452495	336.01	NEB	8.9	4962	10.1	10.22	9.92	610	7287	1.88	2.95
92359850	387.01	NPC	4.2	3880	10.01	10.28	9.61	219	6165	1.26	1.61
123898871	630.01	BEB	4.9	11111	10.08	10.26	9.81	311	6980	1.45	1.74
156987351	476.01	BEB	3.1	6560	9.09	9.26	8.84	246	7104	1.62	2.11
175482273	369.01	BEB	5.5	3229	9.52	9.58	8.92	172	6192	1.26	1.58
350743714	165.01	SB1	7.8	4399	10.01	10.25	9.61	211	6260	1.27	1.51
365781372	627.01	BEB	1.1	5368	10.17	10.3	9.95	640	7127	1.87	3.11

Note.^a NEB: Nearby eclipsing binary; BEB: blended eclipsing binary; SB1: single-lined spectroscopic binary; NPC: transit caused by nearby source that may still be planetary in origin.**Table 12**
Confirmed Planets around Evolved Stars with *T*_{mag} < 10 Not Included in Occurrence Rate Calculation

TIC	TOI	Name	Status	Period (days)	Depth (ppm)	<i>Gaia</i> <i>G</i> (mag)	<i>Gaia</i> <i>B_P</i> (mag)	<i>Gaia</i> <i>R_P</i> (mag)	Distance (pc)	<i>T</i> _{eff} (K)	<i>M</i> _* (<i>M</i> _⊙)	<i>R</i> _* (<i>R</i> _⊙)	References
290131778	123.01	...	P	3.3	3177	8.23	8.43	7.77	162	6234	1.46	2.72	Wang et al. (2019)
231670397	104.01	WASP-73	P	4.1	3586	10.26	10.57	9.82	319	5950	1.21	2.33	Delrez et al. (2014)
339672028	481.01	...	P	10.3	4590	9.85	10.22	9.35	180	5661	0.98	1.8	
410214986	200.01	DS Tuc	P	8.1	3576	8.32	8.7	7.81	44	5466	0.93	0.92	Newton et al. (2019)
452808876	453.01	WASP-82	P	2.7	6400	9.9	10.18	9.49	277	6126	1.27	2.21	West et al. (2016)

ORCID iDs

G. Zhou  <https://orcid.org/0000-0002-4891-3517>
C. X. Huang  <https://orcid.org/0000-0003-0918-7484>
G. Á. Bakos  <https://orcid.org/0000-0001-7204-6727>
J. D. Hartman  <https://orcid.org/0000-0001-8732-6166>
David W. Latham  <https://orcid.org/0000-0001-9911-7388>
S. N. Quinn  <https://orcid.org/0000-0002-8964-8377>
K. A. Collins  <https://orcid.org/0000-0001-6588-9574>
J. N. Winn  <https://orcid.org/0000-0002-4265-047X>
I. Wong  <https://orcid.org/0000-0001-9665-8429>
W. Bhatti  <https://orcid.org/0000-0002-0628-0088>
K. Penev  <https://orcid.org/0000-0003-4464-1371>
A. Bieryla  <https://orcid.org/0000-0001-6637-5401>
M. L. Calkins  <https://orcid.org/0000-0002-2830-5661>
T. Kovács  <https://orcid.org/0000-0002-0697-6050>
Lars A. Buchhave  <https://orcid.org/0000-0003-1605-5666>
M. C. Johnson  <https://orcid.org/0000-0002-5099-8185>
W. D. Cochran  <https://orcid.org/0000-0001-9662-3496>
A. Y. Kniazev  <https://orcid.org/0000-0001-8646-0419>

K. G. Stassun  <https://orcid.org/0000-0002-3481-9052>
B. J. Fulton  <https://orcid.org/0000-0003-3504-5316>
A. Shporer  <https://orcid.org/0000-0002-1836-3120>
N. Espinoza  <https://orcid.org/0000-0001-9513-1449>
D. Bayliss  <https://orcid.org/0000-0001-6023-1335>
M. Everett  <https://orcid.org/0000-0002-0885-7215>
S. B. Howell  <https://orcid.org/0000-0002-2532-2853>
C. Hellier  <https://orcid.org/0000-0002-3439-1439>
D. R. Anderson  <https://orcid.org/0000-0001-7416-7522>
D. J. A. Brown  <https://orcid.org/0000-0003-1098-2442>
N. Schanche  <https://orcid.org/0000-0002-9526-3780>
F. Pozuelos  <https://orcid.org/0000-0003-1572-7707>
M. Gillon  <https://orcid.org/0000-0003-1462-7739>
R. Vanderspek  <https://orcid.org/0000-0001-6763-6562>
J. M. Jenkins  <https://orcid.org/0000-0002-4715-9460>
K. Horne  <https://orcid.org/0000-0003-1728-0304>
N. Narita  <https://orcid.org/0000-0001-8511-2981>
T. G. Tan  <https://orcid.org/0000-0001-5603-6895>
S. Villanueva  <https://orcid.org/0000-0001-6213-8804>

References

- Albrecht, S., Winn, J. N., Johnson, J. A., et al. 2012, *ApJ*, **757**, 18
- Anderson, D. R., Brown, D. J. A., Collier Cameron, A., et al. 2014, arXiv:1410.3449
- Astropy Collaboration, Price-Whelan, A. M., Sipőcz, B. M., et al. 2018, *AJ*, **156**, 123
- Astropy Collaboration, Robitaille, T. P., Tollerud, E. J., et al. 2013, *A&A*, **558**, A33
- Bakos, G., Noyes, R. W., Kovács, G., et al. 2004, *PASP*, **116**, 266
- Bakos, G. Á., Bayliss, D., Bento, J., et al. 2018, arXiv:1812.09406
- Bakos, G. Á., Kovács, G., Torres, G., et al. 2007, *ApJ*, **670**, 826
- Bakos, G. Á., Torres, G., Pál, A., et al. 2010, *ApJ*, **710**, 1724
- Barentsen, G., Hedges, C., Vinícius, Z., & Saunders, N. E. A. 2019, KeplerGO/lightkurve: Lightkurve v1.0b29, v1.0b29, Zenodo, doi:10.5281/zenodo.2565212
- Barkaoui, K., Burdanov, A., Hellier, C., et al. 2019, *AJ*, **157**, 43
- Barnes, J. W. 2009, *ApJ*, **705**, 683
- Barnes, J. W., Linscott, E., & Shporer, A. 2011, *ApJS*, **197**, 10
- Bayliss, D., Gillen, E., Eiglmüller, P., et al. 2018, *MNRAS*, **475**, 4467
- Bayliss, D. D. R., & Sackett, P. D. 2011, *ApJ*, **743**, 103
- Bouma, L. G., Masuda, K., & Winn, J. N. 2018, *AJ*, **155**, 244
- Brandt, T. D., & Huang, C. X. 2015, *ApJ*, **807**, 58
- Brown, T. M., Baliber, N., Bianco, F. B., et al. 2013, *PASP*, **125**, 1031
- Buchhave, L. A., Bakos, G. Á., Hartman, J. D., et al. 2010, *ApJ*, **720**, 1118
- Buchhave, L. A., Latham, D. W., Johansen, A., et al. 2012, *Natur*, **486**, 375
- Burke, C. J. 2008, *ApJ*, **679**, 1566
- Burke, C. J., Christiansen, J. L., Mullally, F., et al. 2015, *ApJ*, **809**, 8
- Castelli, F., & Kurucz, R. L. 2004, arXiv:astro-ph/0405087
- Claret, A. 2017, *A&A*, **600**, A30
- Claret, A., & Bloemen, S. 2011, *A&A*, **529**, A75
- Collier Cameron, A., Guenther, E., Smalley, B., et al. 2010, *MNRAS*, **407**, 507
- Collins, K. A., Collins, K. I., Pepper, J., et al. 2018, *AJ*, **156**, 234
- Crause, L. A., Sharples, R. M., Bramall, D. G., et al. 2014, *Proc. SPIE*, **9147**, 91476T
- Cumming, A., Butler, R. P., Marcy, G. W., et al. 2008, *PASP*, **120**, 531
- Dawson, R. I., & Johnson, J. A. 2018, *ARA&A*, **56**, 175
- Deleuil, M., Aigrain, S., Moutou, C., et al. 2018, *A&A*, **619**, A97
- Delrez, L., Van Grootel, V., Anderson, D. R., et al. 2014, *A&A*, **563**, A143
- Donati, J.-F., Semel, M., Carter, B. D., Rees, D. E., & Collier Cameron, A. 1997, *MNRAS*, **291**, 658
- Dong, S., & Zhu, Z. 2013, *ApJ*, **778**, 53
- Dotter, A. 2016, *ApJS*, **222**, 8
- Dressing, C. D., & Charbonneau, D. 2013, *ApJ*, **767**, 95
- Ekström, S., Georgy, C., Eggenberger, P., et al. 2012, *A&A*, **537**, A146
- Espinosa Lara, F., & Rieutord, M. 2011, *A&A*, **533**, A43
- Foreman-Mackey, D., Hogg, D. W., Lang, D., & Goodman, J. 2013, *PASP*, **125**, 306
- Fressin, F., Torres, G., Charbonneau, D., et al. 2013, *ApJ*, **766**, 81
- Fűrész, G. 2008, PhD thesis, Univ. Szeged
- Gaia Collaboration, Brown, A. G. A., Vallenari, A., et al. 2018, *A&A*, **616**, A1
- Gaudi, B. S., Stassun, K. G., Collins, K. A., et al. 2017, *Natur*, **546**, 514
- Ghezzi, L., Montet, B. T., & Johnson, J. A. 2018, *ApJ*, **860**, 109
- Gillon, M., Anderson, D. R., Collier-Cameron, A., et al. 2013, *A&A*, **552**, A82
- Gould, A., Dorsher, S., Gaudi, B. S., & Udalski, A. 2006, *AcA*, **56**, 1
- Grunblatt, S. K., Huber, D., Gaidos, E., et al. 2018, *ApJL*, **861**, L5
- Guo, X., Johnson, J. A., Mann, A. W., et al. 2017, *ApJ*, **838**, 25
- Hartman, J. D., Bayliss, D., Brahm, R., et al. 2015, *AJ*, **149**, 166
- Hellier, C., Anderson, D. R., Cameron, A. C., et al. 2014, *MNRAS*, **440**, 1982
- Hellier, C., Anderson, D. R., Collier Cameron, A., et al. 2009, *Natur*, **460**, 1098
- Hellier, C., Anderson, D. R., Collier Cameron, A., et al. 2012, *MNRAS*, **426**, 739
- Henden, A. A., Templeton, M., Terrell, D., et al. 2016, AAS Meeting, **225**, 336.16
- Herman, M. K., de Mooij, E. J. W., Huang, C. X., & Jayawardhana, R. 2018, *AJ*, **155**, 13
- Høg, E., Fabricius, C., Makarov, V. V., et al. 2000, *A&A*, **355**, L27
- Howard, A. W., Marcy, G. W., Bryson, S. T., et al. 2012, *ApJS*, **201**, 15
- Huang, C. X., Burt, J., Vanderburg, A., et al. 2018, *ApJL*, **868**, L39
- Huber, D., Chaplin, W. J., Chontos, A., et al. 2019, *AJ*, **157**, 245
- Jehin, E., Gillon, M., Queloz, D., et al. 2011, *Msngr*, **145**, 2
- Jenkins, J. M., Twicken, J. D., McCauliff, S., et al. 2016, *Proc. SPIE*, **9913**, 99133E
- Johnson, J. A., Aller, K. M., Howard, A. W., & Crepp, J. R. 2010, *PASP*, **122**, 905
- Johnson, J. A., Winn, J. N., Bakos, G. Á., et al. 2011, *ApJ*, **735**, 24
- Johnson, M. C., Cochran, W. D., Albrecht, S., et al. 2014, *ApJ*, **790**, 30
- Jones, M. I., Brahm, R., Espinoza, N., et al. 2019, *A&A*, **625**, A16
- Jones, M. I., Jenkins, J. S., Bluhm, P., Rojo, P., & Melo, C. H. F. 2014, *A&A*, **566**, A113
- Kniazev, A. Y., Gvaramadze, V. V., & Berdnikov, L. N. 2016, *MNRAS*, **459**, 3068
- Kniazev, A. Y., Gvaramadze, V. V., & Berdnikov, L. N. 2017, in ASP Conf. Ser. 510, Stars: From Collapse to Collapse, ed. Y. Y. Balega et al. (San Francisco, CA: ASP), 480
- Kovács, G., Bakos, G., & Noyes, R. W. 2005, *MNRAS*, **356**, 557
- Kovács, G., Zucker, S., & Mazeh, T. 2002, *A&A*, **391**, 369
- Kurucz, R. L. 1992, in IAU Symp. 149, The Stellar Populations of Galaxies, ed. B. Barbuy & A. Renzini (Dordrecht: Kluwer), 225
- Lloyd, J. P. 2013, *ApJL*, **774**, L2
- Marcy, G., Butler, R. P., Fischer, D., et al. 2005, *PThPS*, **158**, 24
- Masuda, K. 2015, *ApJ*, **805**, 28
- Masuda, K., & Winn, J. N. 2017, *AJ*, **153**, 187
- Mathur, S., Huber, D., Batalha, N. M., et al. 2017, *ApJS*, **229**, 30
- Maxted, P. F. L., Anderson, D. R., Collier Cameron, A., et al. 2013, *PASP*, **125**, 48
- Mayor, M., Marmier, M., Lovis, C., et al. 2011, arXiv:1109.2497
- Mazeh, T. 2008, in EAS Publications Ser. 29, Tidal Effects in Stars, Planets and Disks, ed. M. J. Goupil & J. P. Zahn (London: EDP Sciences), 1
- McLean, B. J., Greene, G. R., Lattanzi, M. G., & Pirenne, B. 2000, in ASP Conf. Ser. 216, Astronomical Data Analysis Software and Systems IX, ed. N. Manset, C. Veillet, & D. Crabtree (San Francisco, CA: ASP), 145
- Monnier, J. D., Che, X., Zhao, M., et al. 2012, *ApJL*, **761**, L3
- Mulders, G. D., Pascucci, I., & Apai, D. 2015, *ApJ*, **814**, 130
- Natta, A., Testi, L., & Randich, S. 2006, *A&A*, **452**, 245
- Neveu-VanMalle, M., Queloz, D., Anderson, D. R., et al. 2014, *A&A*, **572**, A49
- Newton, E. R., Mann, A. W., Tofflemire, B. M., et al. 2019, *ApJL*, **880**, L17
- Pál, A. 2012, *MNRAS*, **421**, 1825
- Pepper, J., Kuhn, R. B., Siverd, R., James, D., & Stassun, K. 2012, *PASP*, **124**, 230
- Petigura, E. A., Howard, A. W., & Marcy, G. W. 2013, *PNAS*, **110**, 19273
- Petigura, E. A., Marcy, G. W., Winn, J. N., et al. 2018, *AJ*, **155**, 89
- Pollacco, D. L., Skillen, I., Collier Cameron, A., et al. 2006, *PASP*, **118**, 1407
- Queloz, D., Anderson, D. R., Collier Cameron, A., et al. 2010, *A&A*, **517**, L1
- Quinn, S. N., Bakos, G. Á., Hartman, J., et al. 2012, *ApJ*, **745**, 80
- Reffert, S., Bergmann, C., Quirrenbach, A., Trifonov, T., & Künstler, A. 2015, *A&A*, **574**, A116
- Ricker, G. R., Vanderspek, R., Winn, J., et al. 2016, *Proc. SPIE*, **9904**, 99042B
- Rodríguez, J. E., Quinn, S. N., Huang, C. X., et al. 2019, *AJ*, **157**, 191
- Santos, N. C., Israelian, G., Mayor, M., Rebolo, R., & Udry, S. 2003, *A&A*, **398**, 363
- Schanche, N., Collier Cameron, A., Hébrard, G., et al. 2019, *MNRAS*, **483**, 5534
- Schlaflly, E. F., & Finkbeiner, D. P. 2011, *ApJ*, **737**, 103
- Schlaufman, K. C., & Winn, J. N. 2013, *ApJ*, **772**, 143
- Scott, N. J., Howell, S. B., Horch, E. P., & Everett, M. E. 2018, *PASP*, **130**, 054502
- Sharma, S., Stello, D., Buder, S., et al. 2018, *MNRAS*, **473**, 2004
- Shporer, A., Wong, I., Huang, C. X., et al. 2019, *AJ*, **157**, 178
- Siverd, R. J., Collins, K. A., Zhou, G., et al. 2018, *AJ*, **155**, 35
- Skrutskie, M. F., Cutri, R. M., Stiening, R., et al. 2006, *AJ*, **131**, 1163
- Smalley, B., Anderson, D. R., Collier-Cameron, A., et al. 2012, *A&A*, **547**, A61
- Smee, S. A., Barkhouser, R. H., Scharfstein, G. A., et al. 2011, *PASP*, **123**, 87
- Stassun, K. G., Oelkers, R. J., Pepper, J., et al. 2018, *AJ*, **156**, 102
- Stello, D., Huber, D., Grundahl, F., et al. 2017, *MNRAS*, **472**, 4110
- Szabó, G. M., Szabó, R., Benkő, J. M., et al. 2011, *ApJL*, **736**, L4
- Tokovinin, A., Fischer, D. A., Bonati, M., et al. 2013, *PASP*, **125**, 1336
- Triaud, A. H. M. J., Martin, D. V., Ségransan, D., et al. 2017, *A&A*, **608**, A129
- Valenti, J. A., & Fischer, D. A. 2005, *ApJS*, **159**, 141
- Villaver, E., & Livio, M. 2009, *ApJL*, **705**, L81
- Villaver, E., Livio, M., Mustill, A. J., & Siess, L. 2014, *ApJ*, **794**, 3
- von Zeipel, H. 1924, *MNRAS*, **84**, 684
- Wang, J., Fischer, D. A., Horch, E. P., & Huang, X. 2015, *ApJ*, **799**, 229
- Wang, S., Jones, M., Shporer, A., et al. 2019, *AJ*, **157**, 51
- West, R. G., Hellier, C., Almenara, J.-M., et al. 2016, *A&A*, **585**, A126
- Wright, J. T., Marcy, G. W., Howard, A. W., et al. 2012, *ApJ*, **753**, 160
- Zhao, M., Monnier, J. D., Pedretti, E., et al. 2009, *ApJ*, **701**, 209
- Zhou, G., Bakos, G. Á., Bayliss, D., et al. 2019, *AJ*, **157**, 31
- Zhou, G., Latham, D. W., Bieryla, A., et al. 2016, *MNRAS*, **460**, 3376